Effects of Structural Uncertainty on the Dynamic Response of Nearly-Straight Pipes Conveying Fluid: Modeling and Numerical Validation

by

Shrinil Shah

A Thesis Presented in Partial Fulfillment
of the Requirements for the Degree
Master of Science

Approved May 2017 by the
Graduate Supervisory Committee:

Marc Mignolet, Chair
Yongming Liu
Jay Oswald

ARIZONA STATE UNIVERSITY

August 2017

ABSTRACT

This investigation is focused on the consideration of structural uncertainties in nearly-straight pipes conveying fluid and on the effects of these uncertainties on the dynamic response and stability of those pipes. Of interest more specifically are the structural uncertainties which affect directly the fluid flow and its feedback on the structural response, e.g., uncertainties on/variations of the inner cross-section and curvature of the pipe. Owing to the complexity of introducing such uncertainties directly in finite element models, it is desired to proceed directly at the level of modal models by randomizing simultaneously the appropriate mass, stiffness, and damping matrices. The maximum entropy framework is adopted to carry out the stochastic modeling of these matrices with appropriate symmetry constraints guaranteeing that the nature, e.g., divergence or flutter, of the bifurcation is preserved when introducing uncertainty.

To support the formulation of this stochastic ROM, a series of finite element computations are first carried out for pipes with straight centerline but inner radius varying randomly along the pipe. The results of this numerical discovery effort demonstrate that the dominant effects originate from the variations of the exit flow speed, induced by the change in inner cross-section at the pipe end, with the uncertainty on the cross-section at other locations playing a secondary role. Relying on these observations, the stochastic reduced order model is constructed to model separately the uncertainty in inner cross-section at the pipe end and at other locations. Then, the fluid related mass, damping, and stiffness matrices of this stochastic reduced order model (ROM) are all determined from a single random matrix and a random variable. The predictions from this stochastic ROM are found to closely match the corresponding results obtained with the

randomized finite element model. It is finally demonstrated that this stochastic ROM can easily be extended to account for the small effects due to uncertainty in pipe curvature.

TABLE OF CONTENTS

Page

LIST OF TABLES

Table Page

LIST OF FIGURES

Figure Page

Figure Page

Figure Page

Figure Page

CHAPTER ONE

INTRODUCTION

1.1 Background

The stability and dynamics of fluid filled pipes have been the subject of much research over the years motivated by the broad range of applications in heat exchangers, nuclear reactors, medical devices, oil and gas pipelines, etc. This broad literature has been extensively covered and described in the landmark text by Paidoussis [1], in which findings from years of extensive study have been summarized. The text discusses analytical and experimental results and formulations for many configurations of fluid conveying pipes. Another extensive review of the literature has been carried out by Ibrahim [2,3]. With over 400 references, it provides tremendous information regarding modeling, dynamic analysis, and stability regimes for pipes with many types of boundary conditions.

Two particular topics within this large body of work which relate to the current investigation are (i) tapered or conical pipes, i.e., those exhibiting variations of the cross-section and (ii) curved pipes. The consideration of tapered pipes appears to have been initiated by Hannoyer and Paidoussis [4-6] who proceeded with (i) deriving the equations of motion of non-uniform pipes with external and internal flow, (ii) numerically solving the resulting eigenvalue problem with an assumed truncated Fourier series global approximation of the eigenvector, and (iii) performing an experimental validation of the computational results. This extensive investigation remained the state of the art for almost four decades until the recent publications of [7-9]. The focus of these newer studies is primarily on improving the physical understanding of the effects of taper on the

dynamics and stability of the pipes, e.g., Wang et al. [7] have observed that an increase in the taper angle induces a shift of the flutter instability from higher modes to lower modes, thereby forcing the fluid-structure system to become instable at lower velocities. Similar observations have also been drawn in [8, 9].

Contrarily to tapered pipes, curves ones have been the subject of many investigations over a long period with the papers by Misra et al. [10-12], see also [1], providing an excellent summary at that point in time. A key controversy item in the early papers on this topic involved the effects of and need to include the extension of the centerline of the pipe from its no-flow geometry to the statically deformed one under the action of the steady fluid forces. Misra et al. reviewed first two theories: the conventional inextensible theory, in which the centerline of the pipe is assumed to be un-stretched, and the extensible theory, in which the shape of the pipe changes with flow velocity. They then proposed a third theory, the modified inextensible theory, in which the assumption of inextensibility of the centerline is retained but the longitudinal force induced by the steady flow is introduced. Somewhat surprisingly, the matter may not be fully settled yet given the investigation of [13] which started from the nonlinear equations of motion for a semi-circular fluid-conveying pipe and then linearize them to obtain a yet different set of linear equations.

Almost all investigations of the dynamics of curved pipes have focused on arcs of finite (non-small) curvature. Two notable exceptions are the investigations of [14,15] which consider slightly curved pipes conveying fluid with constant flow velocity and proceed to analyze the geometrically nonlinear, large deformations, response of these pipes. The

stability results, performed on the linearized equations, demonstrate that the critical (divergence) velocity shifts to higher values as the curvature increases.

Quite surprisingly given this large body of work, nearly all these studies have been performed under the assumption that the fluid structure system has well defined properties and do not take into consideration the uncertainties in manufacturing process which can lead to variations in the fluid structure system geometry. Notable exceptions are the two investigations [14,15] focusing on shallow curved pipes which explicitly mention the curvature as resulting from "geometric imperfections" although the geometry remains deterministic. The sole stochastic modeling of the uncertainty in pipes and of its propagation to the dynamic response and stability appears to be the very recent investigation of [16], see below for further discussion.

With regards to fluid flow in pipes, there are three main sources of uncertainties in the pipe-fluid system that can be identified. First are the uncertainties associated with the structural problem that have no direct effect on fluid flow. They include the density of the pipe, its Young's modulus, the external shape and diameter (assuming only internal flow), etc. At the opposite end are the fluid only uncertainties, i.e., the density of the fluid, non-uniformity of the flow speed, fluid modeling, which are typically convected along the pipe creating time dependent variations of the system. Finally are the uncertainties on the structure-fluid coupling terms which include variations of the internal shape and diameter of the pipe and of its curvature.

Various probabilistic methods have been developed by which uncertainties associated with design variables (e.g., geometry and/or material properties) can be incorporated in the analysis to capture the effects of their variations on the overall output (e.g., response

and/or stability). In many other applications of structural dynamics besides fluid filled pipes vibrations, the effects of uncertainties on the geometric and/or material properties of the structure have been quite thoroughly investigated, as highlighted by Soize [17]. This reference gives an overview of different methods used for stochastic modeling of uncertainties, types of uncertainties, uncertainty propagation techniques and methods developed to solve these dynamical equations. The aim is ultimately to complement the available, very accurate predictions methods of the response of deterministic systems, e.g., finite element modeling, to account for differences between modeled systems and physical ones.

As discussed in [17], the modeling of uncertainty in structures can be carried in a variety of ways and at various levels, ranging from varying specific local properties of a detailed finite element model (FEM) to modeling the parameters of a global reduced order model (ROM) of the structural response. Given the ubiquitous use of FEM, the consideration of uncertainty within that framework is very natural and such approaches are referred to here as parametric as they affect only specific parameters of the model leaving variations in the others unaccounted for. While some parameters are easily modified, such as the radius, others are not, for example the out of roundness. Since structures are very often analyzed using ROMs, it was proposed, originally in [18], to model the uncertainty directly at the ROM level without formally connecting the uncertain ROM realizations to particular finite element models. Besides its high computationally efficiency, this approach permits the consideration of uncertainty in parameters but also in other properties such as the out of roundness; it has accordingly been referred to as nonparametric. This approach has been applied to a variety of different contexts within

structural dynamics, e.g., linear structural dynamics [18, 19], vibro-acoustics [20, 21], rotor dynamics [22-24], nonlinear structural dynamics [25, 26], nonlinear thermoelastic problems [27], linear viscoelastic structures [28], etc., but also in rigid body dynamics [29, 30] and micromechanics and multiscale modeling, see [17] for extensive review. One important aspect of the nonparametric approach is the selection of the joint probability density function of the ROM parameters which must in particular guarantee that all simulated samples are physically acceptable. To this end, it has been proposed [17, 18] that this function be selected as the one achieving the maximum of the entropy (the Maximum Entropy principle) under the constraint that all properties/conditions on the ROM parameters resulting from the physics of the problem considered be satisfied. For linear structural dynamic problems, the ROM mass and stiffness matrices must be symmetric and positive definite matrices and the consideration of these constraints leads to the "standard" nonparametric approach of [17]. In other problems however, e.g., nonlinear structural dynamics [25, 26] and rotor dynamics [22-24], there are multiple matrices/sets of parameters that must be jointly modeled because they originate from the same aspect of the structure, leading to problem specific variants of the standard nonparametric approach.

1.2 Objectives and Plan

The overall objectives of the present effort are to first clarify the effects, on the pipe stability, of structural uncertainties that affect the fluid induced forces, i.e., variations of the internal shape and diameter of the pipe and of its curvature. To this end, a "computational experiment" is carried out in which the internal diameter of the pipe is

randomly varied along its length and the resulting changes in its stability determined. Next, a global modeling of these uncertainties is developed at the level of a reduced order model using the nonparametric approach. In that, the present investigation parallels the work by Ritto et al. [16] but a notably different formulation is adopted here which results from the observations drawn from the computational experiment.

The next Chapter reviews briefly the governing equations for tapered pipes and describes the formulation and validation of a finite element methodology to predict their stability. Chapter 3 reports on the above computational experiment carried out with the finite element formulation of Chapter 2 on both simply supported and cantilevered pipes with randomly varying inner radii. Next, in Chapter 4, a stochastic reduced order model is formulated to account for the effects of the random taper and its predictions validated in comparison with the results of Chapter 3. Finally, Chapter 5 describes the effects, or more exactly the almost lack thereof, of small random variations in the pipe curvature.

1.3 Dynamic Instabilities in Fluid Filled Systems

The vibrational behavior of pipes depends on the velocity of the fluid it conveys. When this velocity is low, the pipe vibrates as a structural-only multi degree of freedom system exhibiting harmonic motions that are either decaying in time or of constant amplitude as free response. As the flow speed is increased above a particular critical value, it is typically observed that this free response grows in time leading to an unbounded linear response.

As will be described in Chapters 2 and 4, the pipe conveying the fluid can be modeled as the multi degree of freedom system

$$M\,\underline{\ddot{y}} + C\,\underline{\dot{y}} + K\,\underline{y} = \underline{0} \tag{1.1}$$

The corresponding free response is of the form

$$\underline{y} = \underline{\varphi} e^{\lambda t} \tag{1.2}$$

Then, introducing Eq. (1.2) into (1.1) leads to the eigenvalue-type problem

$$\left[M\,\lambda^2 + C\,\lambda + K\right]\underline{\varphi} = \underline{0} \tag{1.3}$$

To determine the eigenvalue λ and eigenvector $\underline{\varphi}$, it is easier to proceed with the state space form equivalent of Eq. (1.1). More specifically, that equation can be rewritten as

$$\hat{B}\,\underline{\dot{\hat{z}}} - \hat{A}\,\underline{\hat{z}} = \underline{0} \tag{1.4}$$

where

$$\hat{B} = \begin{bmatrix} C & M \\ M & 0 \end{bmatrix} \quad \hat{A} = \begin{bmatrix} -K & 0 \\ 0 & M \end{bmatrix} \quad \underline{\hat{z}} = \begin{bmatrix} \underline{y} \\ \underline{\dot{y}} \end{bmatrix} \tag{1.5}$$

Then, assuming a solution of the form

$$\underline{\hat{z}} = \underline{\hat{\varphi}} e^{\lambda t} \tag{1.6}$$

yields the classic generalized eigenvalue problem

$$\hat{A}\,\underline{\hat{\varphi}} = \lambda \hat{B}\,\underline{\hat{\varphi}} \tag{1.7}$$

the solution of which can be determined using standard numerical methods. Since the mass, damping, and stiffness matrices depend on the flow velocity, the eigenvalues will also depend on it.

From the above derivations, it is seen that there are 2 types of instabilities. In the first one, an eigenvalue λ becomes real and positive transitioning through a zero value at a critical flow velocityU_c. This type of instability is referred to as *divergence*. This

phenomenon is commonly observed in pipes supported at both end. When divergence takes place, the eigenvalues are wholly imaginary for $U < U_c$ and then for $U > U_c$ they become wholly real. Divergence is marked by having zero frequency or zero eigenvalue at U_c and is symptomatic of a pitchfork bifurcation.

In the second instability, the real part of an eigenvalue λ becomes positive transitioning through a zero value at a critical flow velocity U_c at which the eigenvalue is then purely imaginary. This instability is referred to as flutter and is commonly seen in pipes with cantilevered boundary conditions. Flutter is characterized by zero structural damping when a pair of eigenvalues cross from $\mathrm{Re}(\lambda) < 0$ to $\mathrm{Re}(\lambda) > 0$ as U is increased, such that at $U = U_C$ the pair of eigenvalues is purely imaginary $\mathrm{Re}(\lambda) = 0$ and $\mathrm{Im}(\lambda) \neq 0$. This type of bifurcation is coined a Hopf bifurcation.

CHAPTER TWO

MODELING OF STRAIGHT PIPES WITH VARYING CROSS SECTION

The dynamics of uniform straight pipes is fairly straightforward and solutions to the system of equations have been extensively studied over the years, e.g., see [1]. However, due to manufacturing tolerances, variations of the internal radius are expected to happen in practice and it is desired in this Chapter to develop a computational tool, i.e., a finite element code that permits the detailed study of the effects of these variations. This tool will then be utilized in the next chapter to obtain data on the overall effects of these variations in inner radius. The core of the formulation, briefly reviewed in the following section, follows the developments of [1, 4-6].

2.1 Equation of Motion of Non-Uniform Pipes

The dynamics of fluid filled pipes with non-uniform flow passage has been studied extensively by Paidoussis and Hannoyer [4-6], see also the summary in [1]. The derivation of the governing equations was developed assuming a slender pipe in which the variations of inner cross-section are axisymmetric, gradual and smooth with respect to the axial coordinate x. Moreover, the complete derivation considers both internal and external flows, both modeled as plug flows, i.e., with constant velocity throughout each cross-section and that remain so as the inner and outer radii are varied. This derivation also includes gravity and pressurization effects.

Under these assumptions, it was found that

$$\frac{\partial^2}{\partial x^2}\left[EI\frac{\partial^2 w}{\partial x^2}\right]-\frac{\rho_i A_i}{2\pi}\frac{dA_i}{dx}\frac{\partial}{\partial x}\left\{\frac{\partial^2 w}{\partial t^2}+2U_i\frac{\partial^2 w}{\partial x\partial t}+U_i^2\frac{\partial^2 w}{\partial x^2}\right\}-\frac{\rho_e A_e}{2\pi}\frac{dA_e}{dx}\frac{\partial}{\partial x}\left\{\frac{\partial^2 w}{\partial t^2}\right\}$$

$$+\rho_i A_i\left\{\frac{\partial^2 w}{\partial t^2}+2U_i\frac{\partial^2 w}{\partial x\partial t}+U_i^2\frac{\partial^2 w}{\partial x^2}\right\}+\rho_e A_e\left\{\frac{\partial^2 w}{\partial t^2}\right\}+\rho_e D_e U_v\frac{\partial w}{\partial t}$$

$$-\left\{\Im(L)+\rho_i A_i U_i\left[U_i-U_i(L)\right]-\int_x^L(\rho_e A_e-\rho_i A_i-m)g\right\}\frac{\partial^2 w}{\partial x^2}$$

$$-\left[(\rho_e A_e-\rho_i A_i-m)g\right]\frac{\partial w}{\partial x}+m\frac{\partial^2 w}{\partial t^2}=0 \qquad (2.1)$$

In Eq. (2.1), $w(x,t)$ denotes the pipe's transverse deflection at axial location *x* and time *t*. Next, the internal and external flow cross-section areas are denoted as A_i and A_e, the structural mass per unit length is *m*, and the flexural rigidity is *EI*. Further, ρ_i and ρ_e are the densities of the internal and external fluids. Finally, the term $\Im(L)$ is referred to as the longitudinal tension and will be discussed further below. In this derivation, the second order terms in $w(x,t)$ have been neglected, as well as transverse shear deformations and rotatory inertia.

In the present investigation, gravity and pressurization effects are neglected and it is assumed that there is no externally imposed tension. Moreover, the fluid conveying system is considered to have no external fluid flow. Then, the governing equation for the transverse displacements reduces from Eq. (2.1) to the following

$$\frac{\partial^2}{\partial x^2}\left[EI\frac{\partial^2 w}{\partial x^2}\right]+m\frac{\partial^2 w}{\partial t^2}-\frac{\rho_i A_i}{2\pi}\frac{dA_i}{dx}\frac{\partial}{\partial x}\left\{\frac{\partial^2 w}{\partial t^2}+2U_i\frac{\partial^2 w}{\partial x\partial t}+U_i^2\frac{\partial^2 w}{\partial x^2}\right\}$$

$$\rho_i A_i\left\{\frac{\partial^2 w}{\partial t^2}+2U_i\frac{\partial^2 w}{\partial x\partial t}+U_i^2\frac{\partial^2 w}{\partial x^2}\right\}-\left\{\rho_i A_i U_i\left[U_i-U_i(L)\right]\right\}\frac{\partial^2 w}{\partial x^2}-\Im(L)\frac{\partial^2 w}{\partial x^2}=0 \qquad (2.2)$$

In this equation, the first term relates to the flexural restoring force or structural stiffness of the pipe while the second represents the structural inertia. The next group of terms arise out of fluid related moments and involve the change in inner radius. The fourth term comprises the core effects of the fluid, i.e., the centrifugal, Coriolis and inertial forces due to the fluid. These terms provide the dominant contributions to the fluid related damping, stiffness and mass. The next, fifth, term is the follower force acting at the end of the pipe resulting from the ejection of the fluid. The last term represents the effects of the longitudinal tension $\Im(L)$. As discussed in [1], it depends on the boundary conditions of the fluid filled system but can generally be neglected under the above assumptions.

With the neglect of the longitudinal tension and a slight regrouping of terms, Eq. (2.2) further simplifies to

$$\frac{\partial^2}{\partial x^2}\left[EI\frac{\partial^2 w}{\partial x^2}\right]-\frac{\rho_i A_i}{2\pi}\frac{dA_i}{dx}\frac{\partial}{\partial x}\left\{\frac{\partial^2 w}{\partial t^2}+2U_i\frac{\partial^2 w}{\partial x\partial t}+U_i^2\frac{\partial^2 w}{\partial x^2}\right\}$$

$$+\rho_i A_i\left\{\frac{\partial^2 w}{\partial t^2}+2U_i\frac{\partial^2 w}{\partial x\partial t}+U_i U_i(L)\frac{\partial^2 w}{\partial x^2}\right\}+m\frac{\partial^2 w}{\partial t^2}=0 \qquad (2.3)$$

2.2 Finite Element Development

2.2.1 Finite Element Formulation

Studying the dynamic behavior of fluid filled pipes with varying inner radius requires solving the partial differential equations (PDE) of Eq. (2.3) with appropriate boundary conditions (see below). Since closed form solutions are not available, it is necessary to proceed with a numerical approach and the finite element method (FEM) is adopted here.

More specifically, a one dimensional finite element modeling of the fluid filled pipe is developed in which each element has two nodes and two degrees of freedom (DOF) per node, thus a total of four degrees of freedom per element. The first nodal DOF correspond to the transverse displacement (w) while the second one is the corresponding rotation (θ). The elemental displacement vector is then

$$\underline{w}^e = [w_1 \quad \theta_1 \quad w_2 \quad \theta_2]^T \tag{2.4}$$

where ^{T} denotes the operation of vector/matrix transposition. The displacement field in that element will then be expressed as

$$w(x,t) = \left[\underline{w}^e(t)\right]^T \underline{N}(x) \tag{2.5}$$

where $\underline{N}(x)$ is a vector of interpolation functions to be selected, see below. Once these functions are known, the mass, damping, and stiffness matrices of the pipe conveying fluid can be constructed. This step will be carried out here using Galerkin method. That is, the approximation of Eq. (2.5) will be introduced in the PDE and the resulting error will be made orthogonal to the interpolation functions selected as trial functions.

To ensure that the nodal displacement and rotations are continuous over the entire pipe, C^1 continuity must be satisfied within each element and this is achieved by selecting the standard Hermitian cubic shape functions as interpolation functions. To proceed next, it is convenient to first map the physical domain of a particular element $x \in [0, l_e]$ to the standard domain $\xi \in [-1,1]$ and this is achieved through the transformation

$$\xi = \frac{2x}{l_e} - 1 \tag{2.6}$$

where x and ξ are referred to as the physical and natural coordinates. With this transformation, the interpolation functions and their first, second, and third derivatives with respect to x are

$$\begin{bmatrix} N_1 \\ N_2 \\ N_3 \\ N_4 \end{bmatrix} = \begin{bmatrix} \frac{1}{4}(1-\xi)^2(2+\xi) \\ \frac{1}{8}l_e(1-\xi)^2(1+\xi) \\ \frac{1}{4}(1+\xi)^2(2-\xi) \\ -\frac{1}{8}l_e(1+\xi)^2(1-\xi) \end{bmatrix} \begin{bmatrix} N_1' \\ N_2' \\ N_3' \\ N_4' \end{bmatrix} = \begin{bmatrix} \frac{3}{2}\left(\frac{\xi^2-1}{l_e}\right) \\ \frac{1}{4}\left(3\xi^2-2\xi-1\right) \\ \frac{3}{2}\left(\frac{-\xi^2+1}{l_e}\right) \\ -\frac{1}{4}\left(1-3\xi^2-2\xi\right) \end{bmatrix} \qquad \text{(2.7.a), (2.7.b)}$$

$$\begin{bmatrix} N_1'' \\ N_2'' \\ N_3'' \\ N_4'' \end{bmatrix} = \begin{bmatrix} \frac{6\xi}{{l_e}^2} \\ \frac{3\xi-1}{l_e} \\ -\frac{6\xi}{{l_e}^2} \\ \frac{3\xi+1}{l_e} \end{bmatrix} \begin{bmatrix} N_1''' \\ N_2''' \\ N_3''' \\ N_4''' \end{bmatrix} = \begin{bmatrix} \frac{12}{{l_e}^3} \\ \frac{6}{{l_e}^2} \\ -\frac{12}{{l_e}^3} \\ \frac{6}{{l_e}^2} \end{bmatrix} \qquad \text{(2.8.a), (2.8.b)}$$

In obtaining the above derivatives of the interpolation functions, it was recognized from Eq. (2.6) that

$$\frac{dx}{d\xi} = \frac{2}{l_e} \qquad (2.9)$$

For future use, it is also noted that the Jacobian for this 1D finite element is

$$Jacobian = J^e = \frac{l_e}{2} \qquad (2.10)$$

2.2.2 Determination of Elemental Matrices

The determination of the elemental mass, damping, and stiffness matrices proceeds by computing the projection of each term in Eq. (2.3) on the 4 interpolation functions of Eq. (2.7.a). The equations below detail the specific contributions of each term to the *ji* element of the corresponding elemental matrix.

Structural stiffness matrix:

$$EI\frac{\partial^4 w}{\partial x^4} \rightarrow \quad E\int_0^{l_e} N_j''^T\, I\, N_i''\, dx = E\int_{-1}^{1} N_j''^T\, I N_i''\, J^e d\xi \tag{2.11}$$

Structural mass matrix:

$$m\frac{\partial^2 w}{\partial t^2} \rightarrow \quad \int_0^{l_e} N_j{}^T\, m\, N_i dx = \int_{-1}^{1} N_j{}^T\, m\, N_i J^e d\xi \tag{2.12}$$

Fluid stiffness matrix

$$\frac{\rho_i A_i}{2\pi}\frac{dA_i}{dx}U_i{}^2\frac{\partial^3 w}{\partial x^3} \rightarrow \quad \frac{\rho_i}{2\pi}\int_0^{l_e} N_j{}^T U_i{}^2 A_i\frac{dA_i}{dx}N_i''' dx = \frac{\rho_i}{2\pi}\int_{-1}^{1} N_j{}^T U_i{}^2 A_i\frac{dA_i}{dx}N'''\, J^e d\xi \tag{2.13}$$

$$\rho_i A_i U_i{}^2\frac{\partial^2 w}{\partial x^2} \rightarrow \quad \rho_i\int_0^{l_e} N_j{}^T A_i U_i{}^2 N_i''\, dx = \rho_i\int_{-1}^{1} N_j{}^T A_i U_i{}^2 N_i'' J^e d\xi \tag{2.14}$$

$$\begin{aligned}\rho_i A_i U_i\left[U_i - U_i(L)\right]\frac{\partial^2 w}{\partial x^2} \rightarrow \quad & \rho_i\int_0^{l_e} N_j{}^T A_i U_i\left[U_i - U_i(L)\right]N_i''\, dx \\ & = \rho_i\int_{-1}^{1} N_j{}^T A_i U_i\left[U_i - U_i(L)\right]N''\, J^e d\xi\end{aligned} \tag{2.15}$$

Fluid damping matrix

$$\frac{\rho_i A_i}{2\pi}\frac{dA_i}{dx}2U_i\frac{\partial^3 w}{\partial x^2 \partial t} \rightarrow \quad \frac{\rho_i}{2\pi}\int_0^{l_e} N_j{}^T 2U_i A_i \frac{dA_i}{dx} N_i'' dx = \frac{\rho_i}{2\pi}\int_{-1}^{1} N_j{}^T 2U_i A_i \frac{dA_i}{dx} N_i'' J^e d\xi \tag{2.16}$$

$$\rho_i 2A_i U_i \frac{\partial^2 w}{\partial x \partial t} \rightarrow \quad \rho_i \int_0^{l_e} N_j{}^T 2A_i U_i N_i' dx = \rho_i \int_{-1}^{1} N_j{}^T 2A_i U_i N_i' J^e d\xi \tag{2.17}$$

Fluid mass matrix

$$\frac{\rho_i A_i}{2\pi}\frac{dA_i}{dx}\frac{\partial^3 w}{\partial x \partial t^2} \rightarrow \quad \frac{\rho_i}{2\pi}\int_0^{l_e} N_j{}^T A_i \frac{dA_i}{dx} N_i' dx = \frac{\rho_i}{2\pi}\int_{-1}^{1} N_j{}^T A_i \frac{dA_i}{dx} N_i' J^e d\xi \tag{2.18}$$

$$\rho_i A_i \frac{\partial^2 w}{\partial t^2} \rightarrow \quad \rho_i \int_0^{l_e} N_j{}^T A_i N_i dx = \rho_i \int_{-1}^{1} N_j{}^T A_i N_i J^e d\xi \tag{2.19}$$

Since the system under consideration is a tapered pipe with internal cross section varying, both the flow velocity and internal area vary along the length of the pipe, but the volumetric flow rate in the pipe remains constant, i.e.,

$$A_i U_i = \text{constant} \tag{2.20}$$

with

$$A_i = \pi r_i^2 \tag{2.21}$$

In the present investigation, it is assumed that the internal radius of the pipe varies linearly between two nodal values, it is thus defined in terms of the natural coordinate by the relation

$$r_i(\xi) = r_{i,left} + \left(r_{i,right} - r_{i,left}\right)\left(\frac{\xi+1}{2}\right) \tag{2.22}$$

Where $r_{i,left}$ and $r_{i,right}$ are the radii at the left end and right end of the element. Using the differentiation rule of Eq. (2.9), one has

$$\frac{dA_i}{dx} = 2\pi r_i \frac{dr_i}{dx} = 2\pi r_i \frac{dr_i}{d\xi}\frac{d\xi}{dx} = 2\pi r_i \frac{\left(r_{i,right} - r_{i,left}\right)}{2}\frac{2}{l_e} \tag{2.23}$$

The integrations involved in Eqs (2.11)-(2.19) were carried out numerically using a Gauss quadrature method with the weights and points taken from [32]. The number of Gauss points n_{GP} can be estimated from the relation given in [33], i.e.,

$$p \le 2n_{GP} - 1 \tag{2.24}$$

Where, p is the order of the polynomial in the integrand. To this end, note that the volumetric flow rate constraint of Eq. (2.20) implies that the flow velocity U_i is not a polynomial of ξ but involves it in the denominator. Thus, a similar term will appear in the integrands of Eqs (2.13)-(2.15). In this light, 12 integration points were selected for each element for all results shown in chapter 3.

2.2.3 Convergence analysis and Numerical Accuracy

A series of computations were carried out to assess the accuracy of the presented finite element results. To this end, the finite element model of the simply supported pipe with a taper angle of 1.2 degree was considered as representative and the effects of the number of elements and Gauss points were first investigated. Specifically, the finite element model was ran initially with 40 elements and 8 Gauss points, then with 40 elements and 12 Gauss points, and finally with 80 element model and 12 Gauss points. The real part and imaginary parts of the eigenvalues obtained for the three cases were found to be very

close to each other, overlaying each other on Figs 1(a) and 1(b). As an indication of the difference, the maximum absolute difference between the 3 sets of normalized real parts of eigenvalues at the arbitrarily selected normalized flow velocity of 2.8040 was found to be 6.425e-5. The corresponding maximum absolute difference for the imaginary parts of eigenvalues at same flow velocity was 5.0e-5.

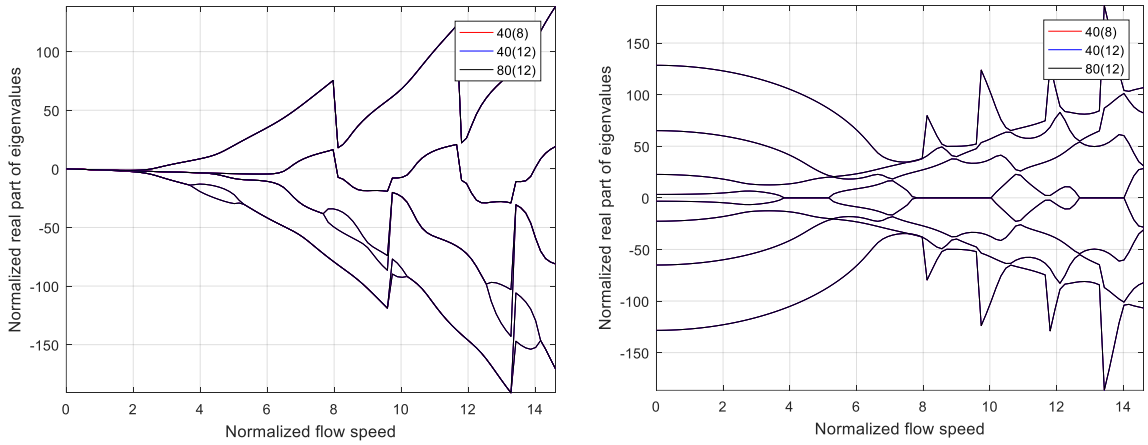

Figure 1. (a) Normalized real part of eigenvalues vs normalized flow speed (b) Normalized imaginary part of eigenvalues vs normalized flow speed, simply supported pipes with taper angle of 1.2 degree, finite element computations with different number of elements and Gauss points

To ensure that the critical velocity was captured accurately from the simulation results, the flow velocity was incremented with a small step size, selected as $1.83\ 10^{-3}$, near the expected first divergence or flutter instability speed. For simply supported cases, the divergence speed was estimated to occur in a particular flow velocity interval if the angle of the curve normalized real part of eigenvalue vs. flow speed exceeded 10 degree between beginning and end points of the interval. When that occurred, the divergence flow speed was recorded as the lower end of the interval. For cantilevered cases, the

flutter speed was obtained by linear interpolation of the normalized real part of eigenvalue between its last negative and first positive values.

2.2.4 Global Finite Element Matrices

After numerical integration, the elemental matrices are scattered into the global finite element matrices. Each of the individual terms contributes to the dynamics as a mass, stiffness, or damping term leading finally to the discretized version of Eq. (2.3) as

$$\left[M_p + M_f(U)\right]\underline{\ddot{w}} + C_f(U)\underline{\dot{w}} + \left[K_p + K_f(U)\right]\underline{w} = 0 \tag{2.25}$$

Where, $\underline{w}$ denotes the time dependent vector of nodal values of the displacement, M_p and M_f are the global structural and fluid mass matrices, C_f is the global fluid damping matrix, and K_p and K_f are the global structural and fluid stiffness matrices. The pipe is assumed here to be undamped without fluid effects.

The particular case of a uniform pipe will also be considered later and in this case, the necessary integrals to determine the elemental matrices can be determined in closed form.

2.2.5 Boundary Conditions

Two different boundary conditions will be considered in the remainder of this thesis: simply supported and cantilevered pipes. For simply supported pipes, the translational degrees of freedom at the two ends, $x = 0$ and $x = L$, are set to zero. That is,

$$w = 0 \text{ at } x = 0 \text{ and } x = L \tag{2.26}$$

In the cantilevered case, the translation and rotation degrees of freedom at the clamp, assumed at $x = 0$ are both set to zero, that is

$$w = 0 \text{ at } x = 0 \text{ and } \frac{\partial w}{\partial x} = 0 \text{ at } x = 0 \tag{2.27}$$

A natural boundary condition exists at the end, $x = L$, of the pipe which is not enforced in the finite element formulation.

2.3 Validation / Verification of FEM model

The finite element formulation and code developed above were validated by comparison against previously published results on the stability of pipes conveying fluid. This validation was carried out for both uniform and constant taper pipes with both boundary conditions, i.e., simply supported and cantilevered pipes. The results of this validation are detailed below, first for the uniform pipe, then for the constantly tapered one.

Following standard practice, the flow velocity and the eigenvalues and flow velocities are normalized by the following quantities

$$U_{norm} = \sqrt{\frac{EI(0)}{\rho_i L^2 A_i(0)}} \tag{2.28}$$

$$\lambda_{norm} = \sqrt{\frac{EI(0)}{L^4\left[\rho_i A_i(0) + \rho_p A_p(0)\right]}} \tag{2.29}$$

where $I(0)$ is the moment of inertia of the pipe at its inlet, and $A_i(0)$ and $A_p(0)$ are the inner and structural cross-section areas at that same location.

For most of the validations, the material properties and geometric parameters were selected as those from the work of [7] on tapered pipes conveying fluid. Specifically, the densities of the fluid (water) and the pipe (silicon) were selected as ρ_i = 1000 kg/m^3 and ρ_p = 2330 kg/m^3. The pipe considered has a length of 200 nm, an inner radius of 8 nm,

and an outer one of 10 nm. Finally, the Young's modulus of the pipe was taken as 130 GPa.

2.3.1 Simply supported uniform pipe

In this case, the finite element (FE) results, real and imaginary parts of eigenvalues plotted against flow speed, were compared to those published in [16]. The plots of normalized eigenvalues vs. normalized flow speeds only depend on the parameter

$$\beta = \frac{\rho_i A_i}{\rho_i A_i + \rho_p A_p} \tag{2.30}$$

The results of [16] were shown for $\beta = 0.24$ and a 40 element model. Then, to allow the closest possible comparison, the number of elements was chosen here as 40 and the outer radius of the pipe was changed to 12.2874 nm to match the value of β. Shown in the Fig. 2 is the comparison for the first four modes and an excellent match is obtained throughout and for all modes. The system undergoes divergence at a critical velocity value of 3.1408 m/s which is very close to the exact value of π [1].

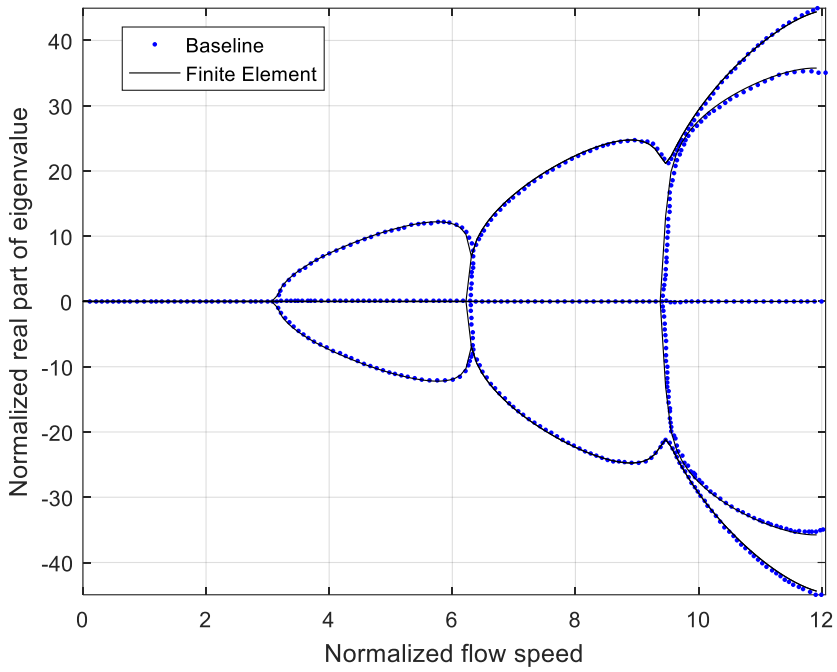

(a)

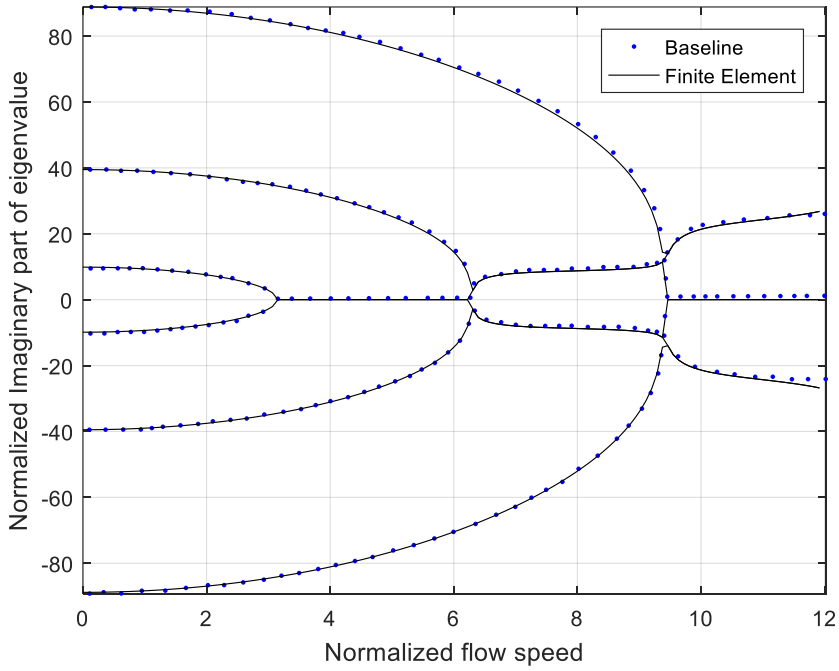

(b)

Figure 2. (a) Normalized real part of eigenvalues and (b) normalized imaginary part of eigenvalues both vs. normalized flow speed, simply supported uniform pipe. Data from [16] ("Baseline") and current predictions ("Finite Element").

2.3.2 Cantilevered uniform pipe

In this case, the FE results for the real and imaginary parts of eigenvalues were validated in comparison with the results of [7], see Fig. 3. The material properties and geometric parameters are stated above and the number of elements considered was 40. Again, an excellent match is obtained.

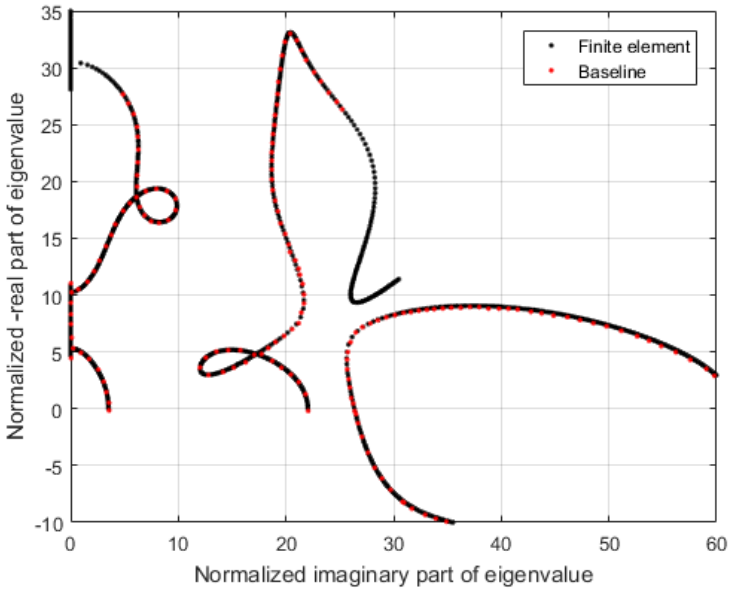

Figure 3. Normalized real part of eigenvalues vs. normalized imaginary part of eigenvalues, cantilevered uniform straight pipe. Data from [7] ("Baseline") and current predictions ("Finite Element")

2.3.3 Cantilevered uniformly tapered pipe

The previous validations have only exercised some of the terms in the finite element model, i.e., none of the terms involving $\frac{dA_i}{dx}$ which was zero in the two previous cases. A comprehensive validation of all terms is now carried out against the results of [7] relevant to the stability of uniformly tapered (or conical) pipes. Their analysis involves taper of both internal and external pipe dimensions, i.e.

$$r_i(x) = r_i(0) - x\tan\alpha \tag{2.31}$$

$$r_o(x) = r_o(0) - x\tan\alpha \tag{2.32}$$

Where α is the taper angle and r_o is the external radius of the pipe. The material properties were selected as above. The validations were carried out for the three different taper angles of α = 0.3, 1.2, and 1.815 degrees and a 40 element finite element model was adopted. Shown in Figs 4-6 are the comparisons of the corresponding present finite element predictions with the results of [7] showing a close agreement. Also presented in [7] are plots of the flutter speed and the corresponding natural frequency as functions of the taper angle α, see Figs 7 and 8. Accordingly, it was desired to also use this data for further validation. To this end, the finite element code was ran with different values of α in the range of angles shown in Figs 7 and 8. For each angle, the real parts of the eigenvalues were then monitored to estimate the flutter speed which was then recorded together with its corresponding natural frequency. These results were then gathered and added to Figs 7 and 8. Again, an excellent match is obtained providing a final confirmation of the correctness of the finite element formulation and code.

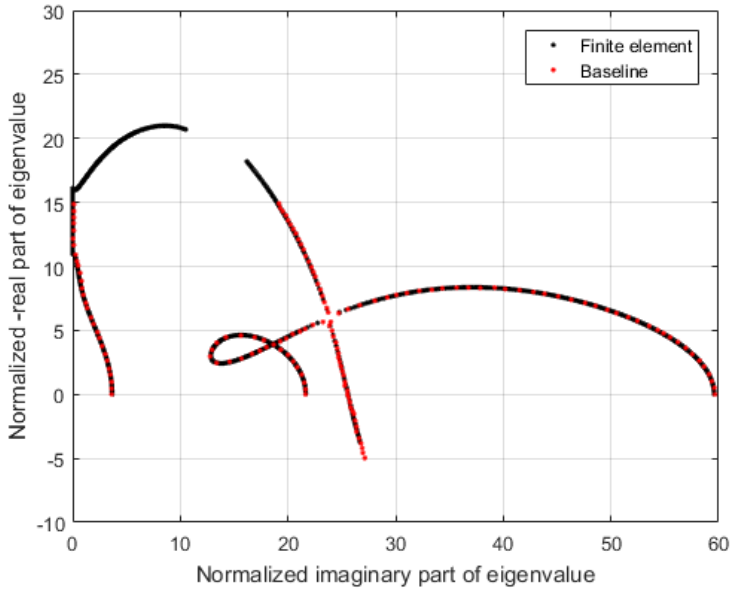

Figure 4. Normalized real part of eigenvalues vs. normalized imaginary part of eigenvalues, cantilevered tapered straight pipe, α = 0.3 degree. Data from [10] ("Baseline") and current predictions ("Finite Element")

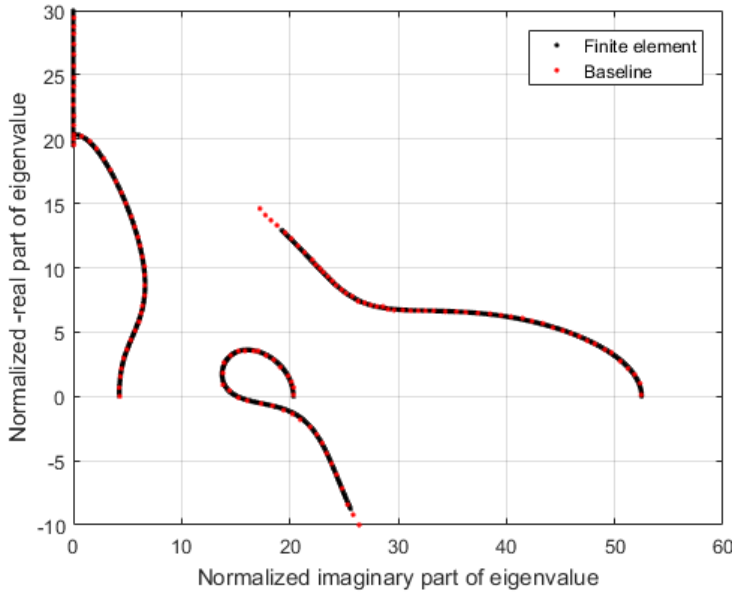

Figure 5. Normalized real part of eigenvalues vs. normalized imaginary part of eigenvalues, cantilevered tapered straight pipe, α = 1.2 degree. Data from [10] ("Baseline") and current predictions ("Finite Element").

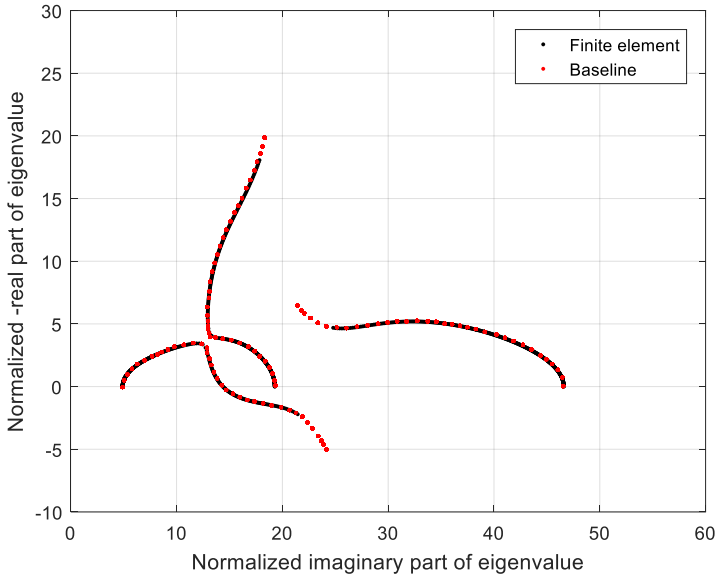

Figure 6. Normalized real part of eigenvalues vs. normalized imaginary part of eigenvalues, cantilevered tapered straight pipe, α = 1.815 degree. Data from [10] ("Baseline") and current predictions ("Finite Element")

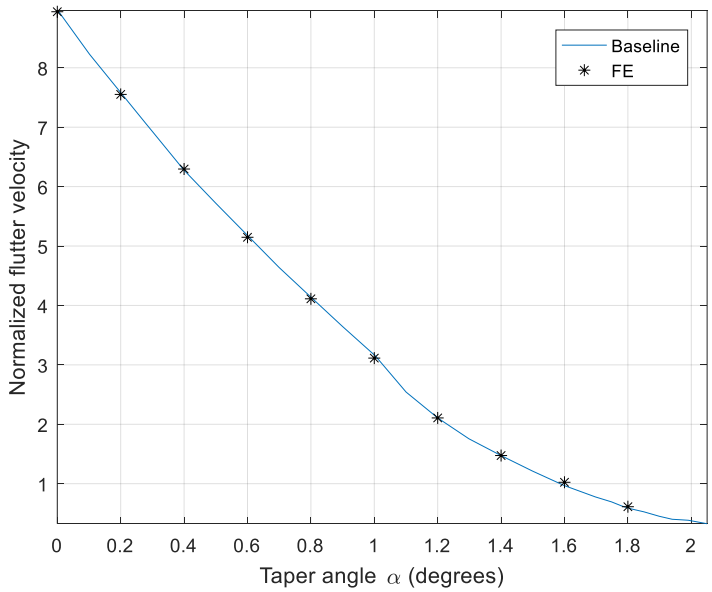

Figure 7. Normalized flutter speed vs. taper angle α. Cantilevered uniformly tapered straight pipe. Data from [7] ("Baseline") and current predictions ("FE").

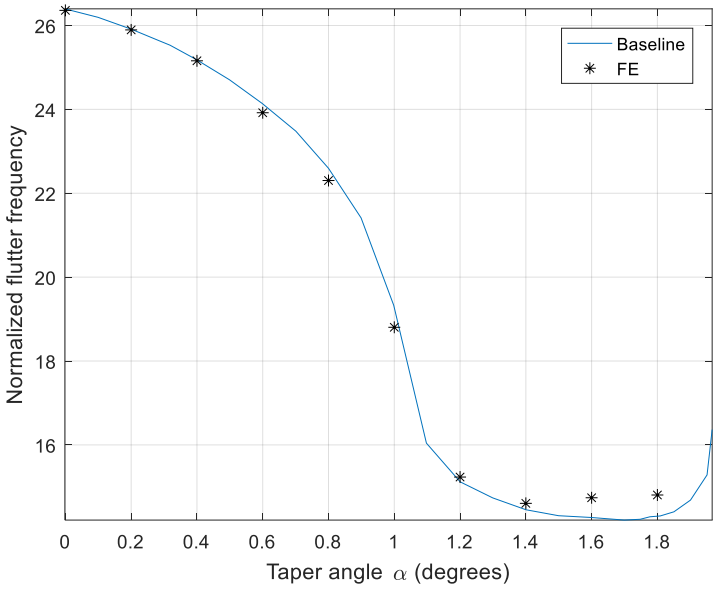

Figure 8. Normalized flutter frequency vs. taper angle α. Cantilevered uniformly tapered straight pipe. Data from [7] ("Baseline") and current predictions ("FE").

2.3.4 Simply supported uniformly tapered pipe

The case of simply supported uniformly tapered pipes does not seem to have been reported in the literature. For completeness, it was nevertheless decided to investigate it, e.g., to confirm the occurrence of divergence. The analysis was carried out for a taper angle of 0.3 degree and shown in Fig. 9 is the normalized real part of the eigenvalues as a function of flow speed. At first glance, it does indeed appear that divergence occurs. On closer inspection, it is seen that some of the eigenvalues have a small positive real part for extremely low velocities. Though small, they would suggest the presence of unstable modes which can cause the system to undergo instability at much lower velocities, almost zero in fact, than the actual divergence velocity. This behavior is clearly unphysical.

It was first questioned whether these non-zero values were the results of finite accuracy computations. To this end, the corresponding eigenvalues for the uniform pipe were also

computed by the same code and compared to those for the tapered case, see Table 1. The significant differences between these two sets of eigenvalues warrant further analysis of the tapered case. To this end, the number of its elements and Gauss points were also varied to assess their potential effects on the eigenvalues shown in Table 1, but these values appear converged. This analysis thus suggests that the observed positive real part of the eigenvalues at low speed is not a numerical problem but results from the problem formulation.

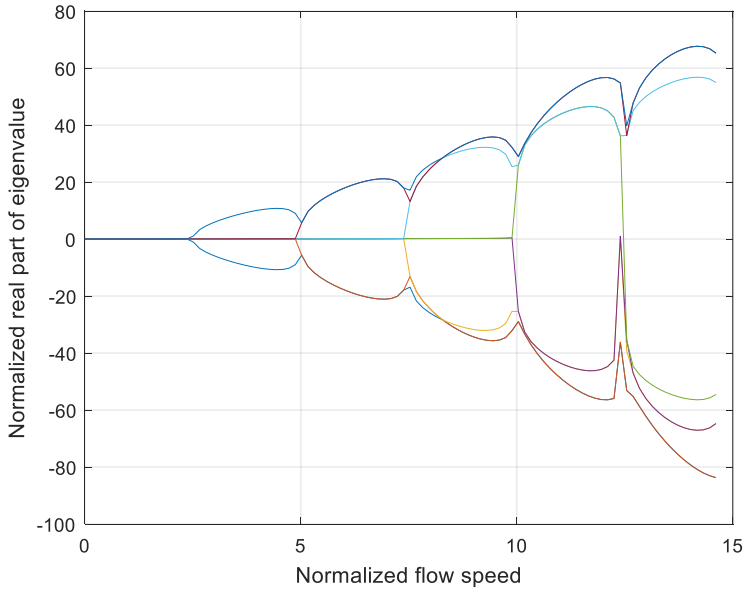

(a)

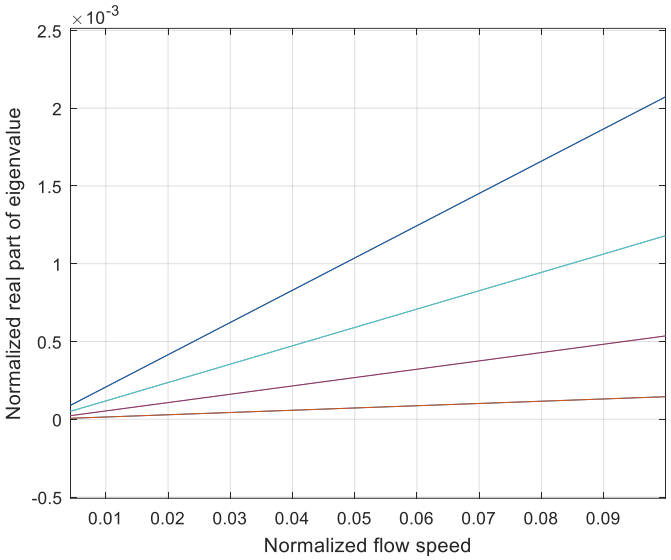

(b)

Figure 9. (a) Normalized real part of eigenvalues vs. normalized flow speed, simply supported uniformly tapered straight pipe, taper angle α = 0.3 degree. (b) Same as (a) zoomed

Table 1. Comparison of real part of eigenvalues of simply supported pipes with constant taper (0.3 degree) and zero taper, Paidoussis and Enhanced models

	Normalized Flow Velocity	**Normalized Real Part of Eigenvalue**			
		Tapered	**Uniform**	**Enhanced 40 elements**	**Enhanced 80 elements**
1	0	8.831 x 10-9	6.167 x 10-9	8.831 x 10-9	8.831 x 10-9
2	0.1476	0.003061	2.037 x 10-9	0.003061	0.003061
3	0.2592	0.006122	3.128 x 10-9	0.006122	0.006122
4	0.4427	0.009184	2.871 x 10-9	0.009184	0.009184
5	0.5903	0.01255	-3.579 x 10-9	0.01255	0.01255
6	1.328	0.0276	4.387 x 10-7	0.0276	0.0276
7	1.476	0.03608	2.498 x 10-9	0.03608	0.03608
8	1.623	0.03377	6.012 x 10-8	0.03377	0.03377

2.4 Enhanced tapered pipe model

To understand the presence of unstable eigenvalues at very low speeds, the derivation of the equation of motion of non-uniform pipes presented in [1] was revisited. In doing so, it was recognized first that the prior equation, Eq. (2.3), is in fact limited to first order terms in the taper (as briefly stated in [1]). On this basis, it was thought that the relatively large positive real part of eigenvalues shown in Fig. 9(b) and Table 1 may result from the truncation of the taper related terms to first order. This hypothesis prompted a complete revisit of the derivation of [1] to include all taper related terms.

With the notations defined in [1], the force balance equations in x and w directions of a small element of pipe conveying fluid are

$$\frac{\partial T}{\partial x} + F_{it} + F_{et} - \left(F_{in} + F_{en}\right)\frac{\partial w}{\partial x} + \frac{\partial}{\partial x}\left(Q\frac{\partial T}{\partial x}\right) + mg = 0 \tag{2.33}$$

$$\frac{\partial Q}{\partial x} + F_{in} + F_{en} - \left(F_{it} + F_{et}\right)\frac{\partial w}{\partial x} + \frac{\partial}{\partial x}\left(T\frac{\partial T}{\partial x}\right) = m\frac{\partial^2 w}{\partial t^2} \tag{2.34}$$

Similarly, the moment balance equation is

$$Q + \frac{\partial}{\partial x}\left(EI\frac{\partial^2 w}{\partial x^2}\right) + \frac{\partial \mathrm{M}_f}{\partial x} = 0 \tag{2.35}$$

In Eqs (2.33)-(2.34), F_{it} and F_{in} are the tangential and normal components of the fluid-pipe interaction forces associated with the internal flow and F_{et} and F_{en} are their counterparts for the external fluid flow. The symbol Q denotes the transverse shear force and M_f is the fluid related moment associated with the external and internal flow. Other quantities in the equation are as defined in Section 2.1.

The force balance equations on the fluid element are [1]

$$F_{it} - F_{in}\frac{\partial w}{\partial x} = -\frac{\partial}{\partial x}\left(\rho_i A_i\right) + \rho_i A_i g - \rho_i A_i U_i \frac{dU_i}{dx} \tag{2.36}$$

$$F_{in} - F_{it}\frac{\partial w}{\partial x} = -\frac{\partial}{\partial x}\left(\rho_i A_i \frac{\partial w}{\partial x}\right) + \rho_i A_i D^2 w \tag{2.37}$$

where,

$$D^2 w = \left[\frac{\partial^2 w}{\partial t^2} + 2U_i \frac{\partial^2 w}{\partial x \partial t} + U_i \frac{\partial}{\partial x}\left(U_i \frac{\partial w}{\partial x}\right)\right] \tag{2.38}$$

Since for the current analysis no external fluid is acting in the system, the equation for the external forces has been neglected.

The evaluation of M_f is stated in [1] as "quite tedious" pointing to the derivation of [4]. A review of this derivation has suggested that it holds regardless of the taper magnitude, i.e., is not simplified to first order. Thus,

$$-\frac{\partial \mathrm{M}_f}{\partial x} = \frac{\rho_i A_i}{2\pi}\frac{dA_i}{dx} D^2 w + \frac{\rho_e A_e}{2\pi}\frac{dA_e}{dx}\frac{\partial^2 w}{\partial t^2} \tag{2.39}$$

Combining the above equations in the present case without external flow or gravity leads to

$$\frac{\partial^2}{\partial x^2}\left[EI\frac{\partial^2 w}{\partial x^2}\right] - \frac{\partial}{\partial x}\left[\frac{\rho_i A_i}{2\pi}\frac{dA_i}{dx} D^2 w\right] + \rho_i A_i\left[D^2 w - U_i \frac{dU_i}{dx}\frac{\partial w}{\partial x}\right]$$

$$-\left[\rho_i A_i U_i^2 - \rho_i A_i U_i U_i (L)\right]\frac{\partial^2 w}{\partial x^2} + m\frac{\partial^2 w}{\partial t^2} = 0 \tag{2.40}$$

Or, after expanding the $D^2 w$ term according to Eq. (2.38)

$$\frac{\partial^2}{\partial x^2}\left[EI\frac{\partial^2 w}{\partial x^2}\right] - \frac{\partial}{\partial x}\left[\frac{\rho_i A_i}{2\pi}\frac{dA_i}{dx}\left(\frac{\partial^2 w}{\partial t^2} + 2U_i \frac{\partial^2 w}{\partial x \partial t} + U_i^2 \frac{\partial^2 w}{\partial x^2} + U_i \frac{dU_i}{dx}\frac{\partial w}{\partial x}\right)\right]$$

$$\rho_i A_i\left(\frac{\partial^2 w}{\partial t^2}+2U_i\frac{\partial^2 w}{\partial x\partial t}\right)+\rho_i A_i U_i U_i(L)\frac{\partial^2 w}{\partial x^2}+m\frac{\partial^2 w}{\partial t^2}=0 \tag{2.41}$$

The difference between this equation and Eq. (2.3) are the terms in the second bracket which are

$$\begin{aligned}
&\frac{\partial}{\partial x}\left[\frac{\rho_i A_i}{2\pi}\frac{dA_i}{dx}\left(\frac{\partial^2 w}{\partial t^2}+2U_i\frac{\partial^2 w}{\partial x\partial t}+U_i^2\frac{\partial^2 w}{\partial x^2}+U_i\frac{dU_i}{dx}\frac{\partial w}{\partial x}\right)\right]\\
&=\frac{\rho_i A_i}{2\pi}\frac{dA_i}{dx}\left(\frac{\partial^3 w}{\partial x\partial t^2}+2U_i\frac{\partial^3 w}{\partial x^2\partial t}+U_i^2\frac{\partial^3 w}{\partial x^3}\right)+\frac{\rho_i A_i}{2\pi}\left(\frac{dA_i}{dx}\right)^2\frac{\partial^2 w}{\partial t^2}+\frac{\rho_i A_i}{2\pi}\frac{d^2 A_i}{dx^2}\frac{\partial^2 w}{\partial t^2}\\
&+\frac{\rho_i}{2\pi}(2A_i U_i)\frac{d^2 A_i}{dx^2}\frac{\partial^2 w}{\partial x\partial t}+\frac{\rho_i}{2\pi}\left(A_i U_i^2\right)\frac{d^2 A_i}{dx^2}\frac{\partial^2 w}{\partial x^2}+\frac{\rho_i}{2\pi}(A_i U_i)\frac{d^2 A_i}{dx^2}\frac{\partial^2 w}{\partial x^2}\\
&+\frac{\rho_i}{2\pi}(A_i U_i)\frac{dU_i}{dx}\frac{dA_i}{dx}\frac{\partial^2 w}{\partial x^2}+\frac{\partial}{\partial x}\left[\frac{\rho_i A_i}{2\pi}\frac{dA_i}{dx}U_i\frac{dU_i}{dx}\frac{\partial w}{\partial x}\right]
\end{aligned} \tag{2.42}$$

A comparison of the above terms with their counterparts from Eq. (2.3) shows that the first group of terms in Eq. (2.42) is indeed present in Eq. (2.3) but none of the others is. In evaluating them, note that

$$\frac{dU_i}{dx}=-\frac{U_i}{A}\frac{dA_i}{dx}=-\frac{\rho}{2\pi}\left(\frac{dA_i}{dx}\right)^2 U_i^2\frac{\partial^2 w}{\partial x^2} \tag{2.43}$$

Moreover, the last term of Eq. (2.42) can be evaluated as follows

$$\frac{\partial}{\partial x}\left[\frac{\rho_i A_i}{2\pi}\frac{dA_i}{dx}U_i\frac{dU_i}{dx}\frac{\partial w}{\partial x}\right]=\frac{\rho_i}{2\pi}(A_i U_i)\left(\frac{dA_i}{dx}\frac{dU_i}{dx}\right)\frac{\partial^2 w}{\partial x^2}+\frac{\rho_i}{2\pi}(A_i U_i)\frac{\partial}{\partial x}\left(\frac{dA_i}{dx}\frac{dU_i}{dx}\right)\frac{\partial w}{\partial x} \tag{2.44}$$

where

$$\frac{\partial}{\partial x}\left(\frac{dA_i}{dx}\frac{dU_i}{dx}\right)=-\frac{2U_i}{A_i^2}\left[A_i\left(\frac{dA_i}{dx}\right)\left(\frac{d^2 A_i}{dx^2}\right)-\left(\frac{dA_i}{dx}\right)^3\right] \tag{2.45}$$

The enhanced model governing equation, Eq. (2.41), was implemented in a finite element format following the steps of section 2.2 with the following terms contributing to the structural and fluid mass, fluid damping, and structural and fluid stiffness.

$$M_p : m\frac{\partial^2 w}{\partial t^2} \tag{2.46}$$

$$M_f : \frac{\rho_i A_i}{2\pi}\frac{dA_i}{dx}\frac{\partial^3 w}{\partial x \partial t^2} + \rho_i A_i \frac{\partial^2 w}{\partial t^2} + \frac{\rho_i A_i}{2\pi}\left(\frac{dA_i}{dx}\right)^2 \frac{\partial^2 w}{\partial t^2} + \frac{\rho_i A_i}{2\pi}\frac{d^2 A_i}{dx^2}\frac{\partial^2 w}{\partial t^2} \tag{2.47}$$

$$C_f : \frac{\rho_i A_i}{2\pi}\frac{dA_i}{dx} 2U_i \frac{\partial^3 w}{\partial x^2 \partial t} + 2\rho_i A_i U_i \frac{\partial^2 w}{\partial x \partial t} + \frac{\rho_i A_i}{2\pi} 2A_i U_i \frac{d^2 A_i}{dx^2}\frac{\partial^2 w}{\partial x \partial t} \tag{2.48}$$

$$K_p : EI\frac{\partial^4 w}{\partial x^4} \tag{2.49}$$

$$\begin{aligned} K_f : & \frac{\rho_i A_i}{2\pi}\frac{dA_i}{dx} U_i^2 \frac{\partial^3 w}{\partial x^3} + \rho_i A_i U_i^2 \frac{\partial^2 w}{\partial x^2} + \rho_i A_i U_i \left[U_i - U_i(L)\right]\frac{\partial^2 w}{\partial x^2} \\ & \frac{\rho_i}{2\pi}\left(A_i U_i^2\right)\frac{d^2 A_i}{dx^2} U_i^2 \frac{\partial^2 w}{\partial x^2} + \rho_i A_i U_i \frac{d^2 A_i}{dx^2}\frac{\partial^2 w}{\partial x^2} + \frac{\rho_i}{2\pi} A_i U_i \frac{dU_i}{dx}\frac{dA_i}{dx}\frac{\partial^2 w}{\partial x^2} \\ & \frac{\rho_i}{2\pi}\left(A_i U_i\right)\frac{dA_i}{dx}\frac{dU_i}{dx}\frac{\partial^2 w}{\partial x^2} + \frac{\rho_i}{2\pi} A_i U_i \frac{\partial}{\partial x}\left[\frac{dA_i}{dx}\frac{dU_i}{dx}\right]\frac{\partial w}{\partial x} \end{aligned} \tag{2.50}$$

2.5 Comparison of Paidoussis and Enhanced Models

The predictions from the finite element code implementing the enhanced model were compared to those obtained from the one described in Section 2.2 and based on the Paidoussis model, i.e., Eq. (2.3) for the simply supported pipe of section 2.3.4. It was observed that the results are almost perfectly in agreement over the entire speed range even at low flow speeds, see Table 1. These results demonstrate that the presence of

eigenvalues with small real parts at low flow speeds is not due to the retention of only the linear terms in taper in the Paidoussis model and thus remains, at this point, an unresolved issue.

CHAPTER THREE

RANDOMLY TAPERED PIPES: DISCOVERY EFFORT

This chapter focuses on reporting the results of "computational experiments" carried out with the finite element code formulated and validated in Chapter 2 but in which the inner radii of the tapered pipes were randomly varied. These experiments are performed first to analyze and understand the effects of random variations in internal radius on the overall stability of the fluid conveying pipe. The second objective of these experiments is to generate the data for validation and verification of the stochastic reduced order models developed in the following chapter.

A series of numerical calculations were carried out for randomly tapered pipes with simply supported and cantilevered boundary conditions. For the analysis, the finite element code consisted of all the terms that are defined in section (2.4). Discussions by Paidoussis [1] have demonstrated that the behavior of cantilevered tapered pipes is strongly dependent on the exit velocity $U_i(L)$ which is explicitly present in Eq. (2.3). Note that this velocity is solely dictated by the inner radius at that location. On this basis, three cases were identified:

Option 1: Numerical computations were carried for pipes with only the exit velocity varying. This condition is ensured by randomizing only the inner radius at the last node of the finite element mesh and keeping it equal to the mean model value at all the other nodes. The external radius of the pipe is constant throughout the length of the pipe.

Option 2: Numerical computations were carried for pipes with the radius varying at every node of the finite element model (except at the inlet, see below). The external radius is however assumed to be constant throughout the pipe.

Option 3: Numerical computations were carried for pipes in which the internal radius is randomized throughout the length of the pipe except at the end and at the inlet (see below). The radius at the end of the pipe is fixed to its value at the inlet and the external radius is constant throughout the pipe.

The inner radius at the inlet node was kept constant for convenience so that the various samples simulated could be compared based on the same flow speed at the inlet as opposed to matching the volumetric flow rate. Since these results are intended to provide baseline data to validate the stochastic ROM of Chapter 4, the mass and stiffness matrices of the pipe without flow, M_p and K_p, were kept constant in the simulations. Thus, the results presented here describe the effect of random variations of the fluid related forces on the pipe stability only.

The inner radii were first modeled as independent truncated Gaussian random numbers of mean equal to the mean model and specified standard deviation. The simulated values were limited to ± 4 standard deviations to avoid the occurrence of unphysical, very large changes of the inner radius. The computations were also repeated with uniformly distributed random inner radii of identical mean and standard deviation to assess the effects, or lack thereof, of the distribution of these properties. For the simply supported case, the coefficient of variation of the inner radius was assumed to be 1.5%. Similarly, it was considered to be 0.75% for cantilevered pipes.

In judging the magnitude of the induced variations of geometry, it is useful to evaluate the corresponding standard deviations of taper angle. From Eq. (2.31), it is seen that the taper angle α_i in the element *i* is such that

$$\tan\alpha_i = \frac{r_i(x_{i+1}) - r_i(x_i)}{x_{i+1} - x_i} \tag{3.1}$$

When the radii at the beginning and end of the elements are independent, one obtains assuming the taper angle small

$$\sigma_{\alpha_i} \approx \frac{\sqrt{2}\,\sigma_{r_i}\,M}{L} \tag{3.2}$$

where σ_{α_i} and σ_{r_i} are the standard deviations of the taper angle and radius, *M* is the number of elements and *L* is the length of the pipe. Thus, the variations of radius stated above induce here standard deviations of element taper angle equal to 1.9 and 1 degree in the simply supported and cantilevered cases.

For the analysis, an initial computation was carried for the base or mean model. Then, using a 40 element mesh, 400 Monte Carlo simulations were performed for each of the cases described above. For comparison and future use, the plots of the real and imaginary parts of the eigenvalues vs. flow velocity as well as the estimated probability density functions of the critical velocities (flutter and divergence) are presented in Figs 10-15. The variations of the eigenvalues is reflected on these figures by the uncertainty band shown in yellow which corresponds, at each flow velocity, to the interval spanning the 5th to 95th percentiles of the computed real/imaginary parts of the eigenvalues.

From these figures, it is concluded that:

i. The most significant effect of the change in radius is through the exit velocity $U_i(L)$, compare the results for options 1 and 2. In fact, see option 3, it does not appear that the variation of radius inside the pipe domain, i.e., $x \in (0, L)$ induces much change in the pipe response, at least for the independent random variations, Gaussian or uniform, of radius considered here.

ii. The distributions of the critical speed are very similar in the Gaussian and uniform case in option 3, when there is a large number of random variables describing the geometry. Moreover, these distributions are Gaussian-like. These observations likely results from a central limit type situation, especially considering the small magnitude of the effects of variation in radius in that option. On the contrary, in options 1 and 2, the distribution of the critical speed strongly reflects the distribution of inner radius. This finding is expected since from (i) it was concluded that $U_i(L)$ is dominant. So, the critical speed can effectively be recognized as a mapping of the inner radius at the pipe end. Given the relatively small changes in critical speed, this mapping is approximately linear and thus the probability density function of the critical speed is similar to that of the inner radius as observed.

iii. There is a small shift of the mean critical speed which is more visible in option 3 because the variations in this speed are smaller. To facilitate this observation, the mean model value is indicated by a red triangle in Figs 10-15 (e) and (f).

The small level of variability observed in option 3 was unexpected and it was questioned whether it could be the result of the assumed independence, in the above computations, of the nodal values of the inner radius. To assess this possibility and study more completely

the effects of variations of inner radii, these random variables were next assumed to be Gaussian distributed but exponentially correlated, that is with

$$E\left[r_i\left(x_j\right)r_i\left(x_l\right)\right]=\sigma_{r_i}\,\exp\left(-\left|x_j-x_l\right|/\lambda\right) \tag{3.3}$$

where λ is the correlation length. Realizations of the inner radii were generated by first forming the covariance matrix V of jl element

$$V_{jl}=E\left[r_i\left(x_j\right)r_i\left(x_l\right)\right] \tag{3.4}$$

In forming this matrix, it was convenient (see below) to stack the inner radii in the following order of nodes: 1, 41, 2, 3, ..., 40. Next, a Cholesky decomposition of the covariance matrix was performed yielding the lower triangular matrix $\hat{L}$ such that

$$V=\hat{L}\,\hat{L}^T \tag{3.5}$$

Finally, samples of the inner radii stacked in the vector $\underline{r}$ were obtained as

$$\underline{r}=\hat{L}\,\underline{z}+\bar{\underline{r}} \tag{3.6}$$

where $\underline{z}$ denotes a vector of independent standard Gaussian random variables and $\bar{\underline{r}}$ is the vector of inner radii for the mean model. To ensure that the inner radii at the first and last node were kept constant to their mean values, the first two components of the vector $\underline{z}$ were simply constrained to be zero.

The above simulation was performed for a series of values of the correlation length λ. For each of these, 300 sets of inner radii were generated and used in the finite element code to estimate, in option 3, the flutter speed of the corresponding cantilevered pipe. This data was then reduced to the mean, standard deviation, and probability density of the divergence/flutter speed which are plotted as functions of the correlation length on Figs

16 and 17 for the cantilevered boundary conditions and Figs 18 and 19 for the simply supported ones.

While the behavior of the mean critical speed is similar for both boundary conditions, i.e., sharp initial increase with increasing correlation length then leveling off, opposite behaviors are seen on the plots of the standard deviation. For the cantilevered case, the standard deviation first rises sharply to achieve a maximum at a correlation length approximately equals to 1/4 of the pipe length then decreases steadily. For the simply supported pipe, the standard deviation first decrease until the correlation length approximately equals the same 1/4 of the pipe length, where it is almost zero, then increases and levels off.

In analyzing these trends, it should first be recognized that the standard deviation of the element taper angle, derived as in Eqs (3.1) and (3.2), is

$$\sigma_{\alpha_i} \approx \frac{\sqrt{2}\,\sigma_{r_i} M}{L}\left\{1-\exp\left[-\left(x_{i+1}-x_i\right)/\lambda\right]\right\} \tag{3.7}$$

which is monotonically decreasing with increasing correlation length λ as expected since the evolution of the inner radius along the pipe becomes smoother. Consequently, all taper related term in Eq. (2.3) or (2.42) are expected to decrease on average as the correlation length is increased at constant standard deviation σ_{r_i}. Short correlation variations, on the other hand, are expected to be "averaged out" in the global character of the instability as is confirmed by the Gaussian like probability density functions of the divergence/flutter speed obtained in option 3, see Figs 12 and 15, regardless of the distribution of the inner radius (uniform or truncated Gaussian). Accordingly, it is believed that there are two competing mechanisms at work as the correlation length is increased, one of growth and one of

decrease, the interplay of which leads to an optimum, maximum or minimum, of the standard deviation of the critical speed as observed on Figs 16(b) and 18(b).

In concluding this analysis, note that the peak coefficient of variation of the flutter speed in the cantilevered case is larger than its counterpart for the divergence speed of the simply supported pipe even though the standard deviation of inner radius is smaller in the former case than in the latter one. Thus, cantilevered pipes are more sensitive to inner radius variations than simply supported ones.

Finally, it should be recognized that even the peak standard deviation of flutter speed observed on Fig. 16(b), i.e., 9×10^{-3}, is much smaller than its option 1 counterpart, i.e., 0.1107, so that the earlier stated dominance of the effects of the exit flow speed $U(L)$ still remains valid.

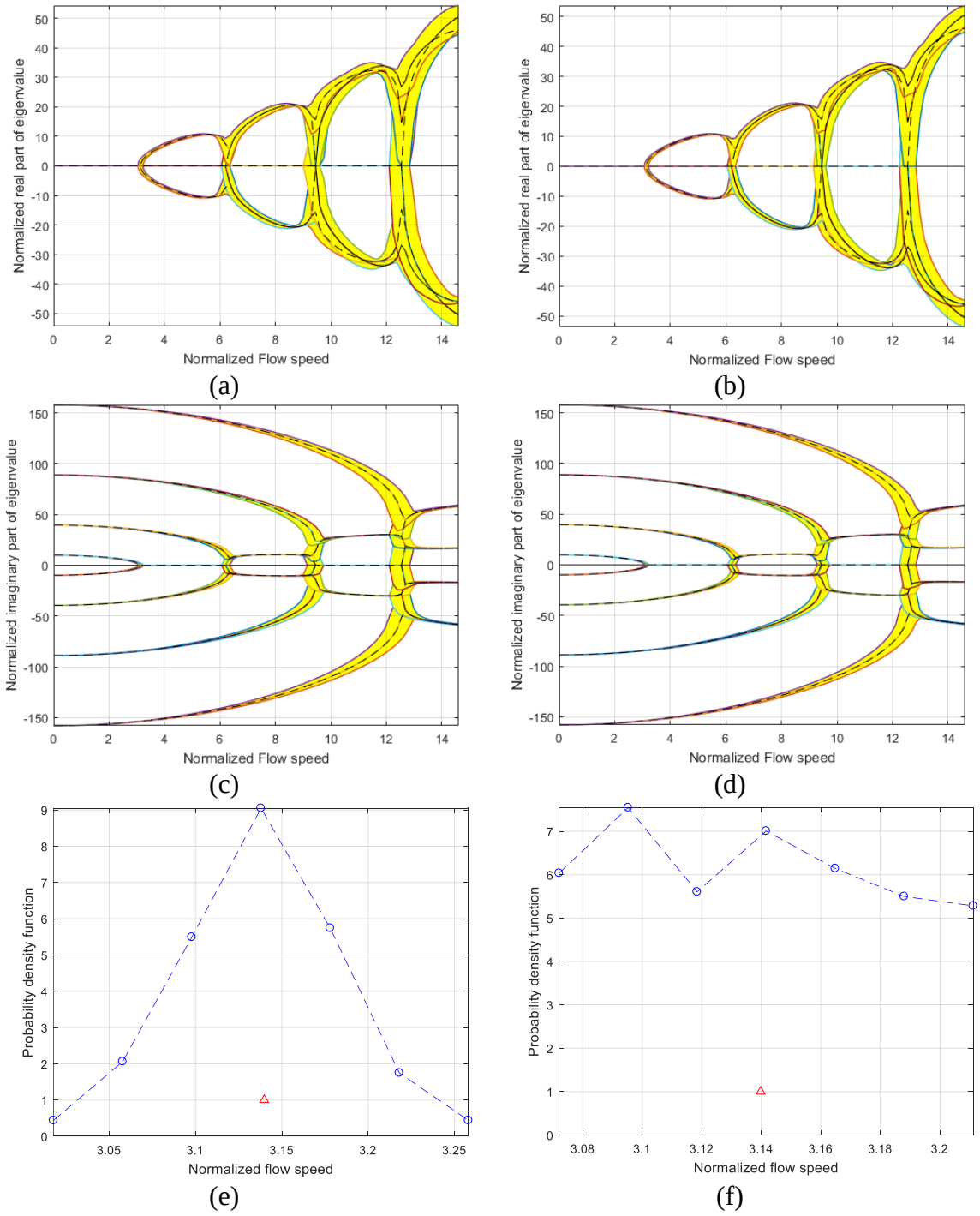

Figure 10. (a),(b) Normalized real part of eigenvalues vs. normalized flow speed; (c),(d) normalized imaginary part of eigenvalues vs. normalized flow speed; (e),(f) probability density function of divergence speed. Mean model shown as "--". (a),(c),(e) Gaussian and (b),(d),(f) uniform inner radius distribution for simply supported pipes - option 1

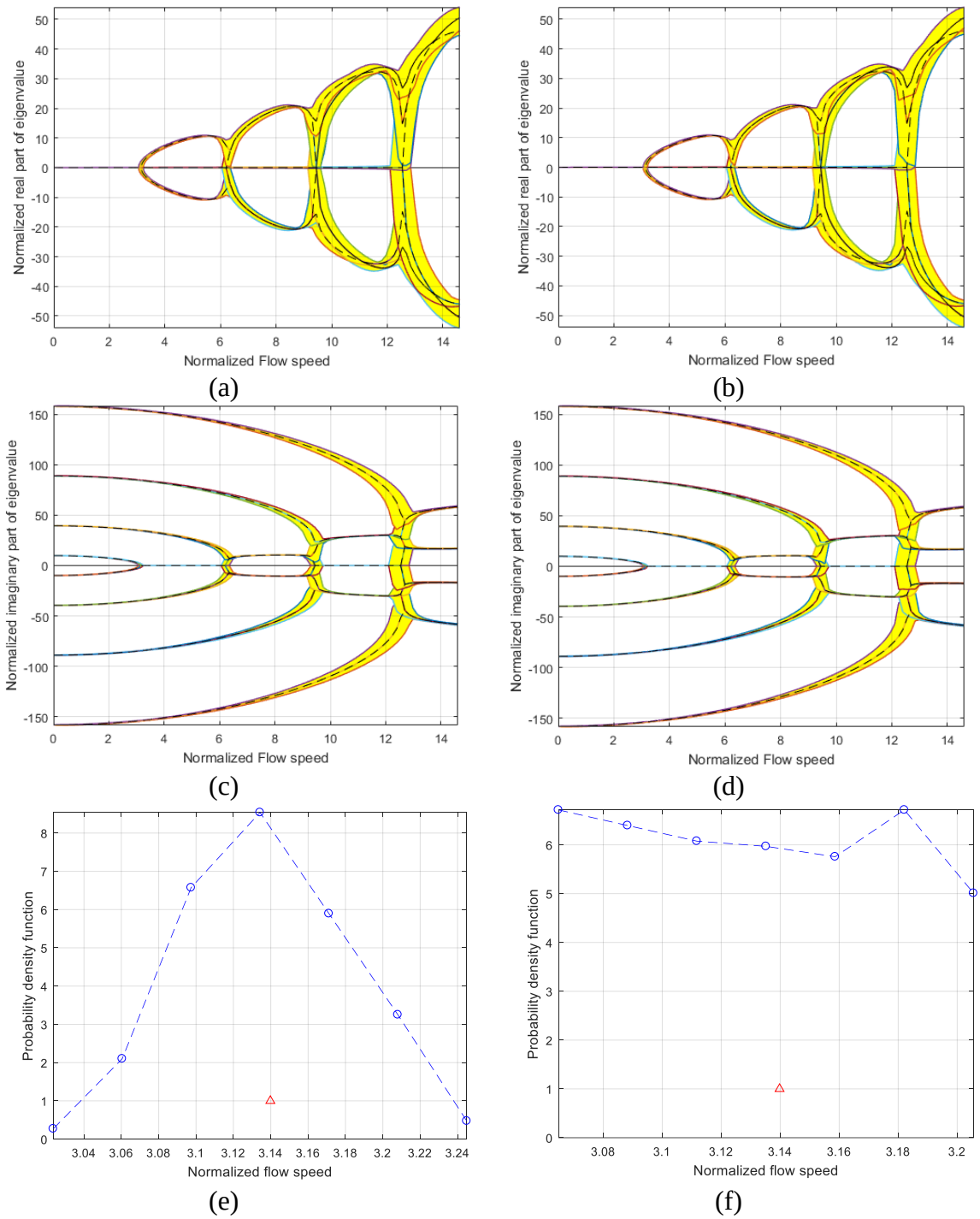

Figure 11. (a),(b) Normalized real part of eigenvalues vs. normalized flow speed; (c),(d) normalized imaginary part of eigenvalues vs. normalized flow speed; (e),(f) probability density function of divergence speed. Mean model shown as "--". (a),(c),(e) Gaussian and (b),(d),(f) uniform inner radius distribution for simply supported pipes - option 2

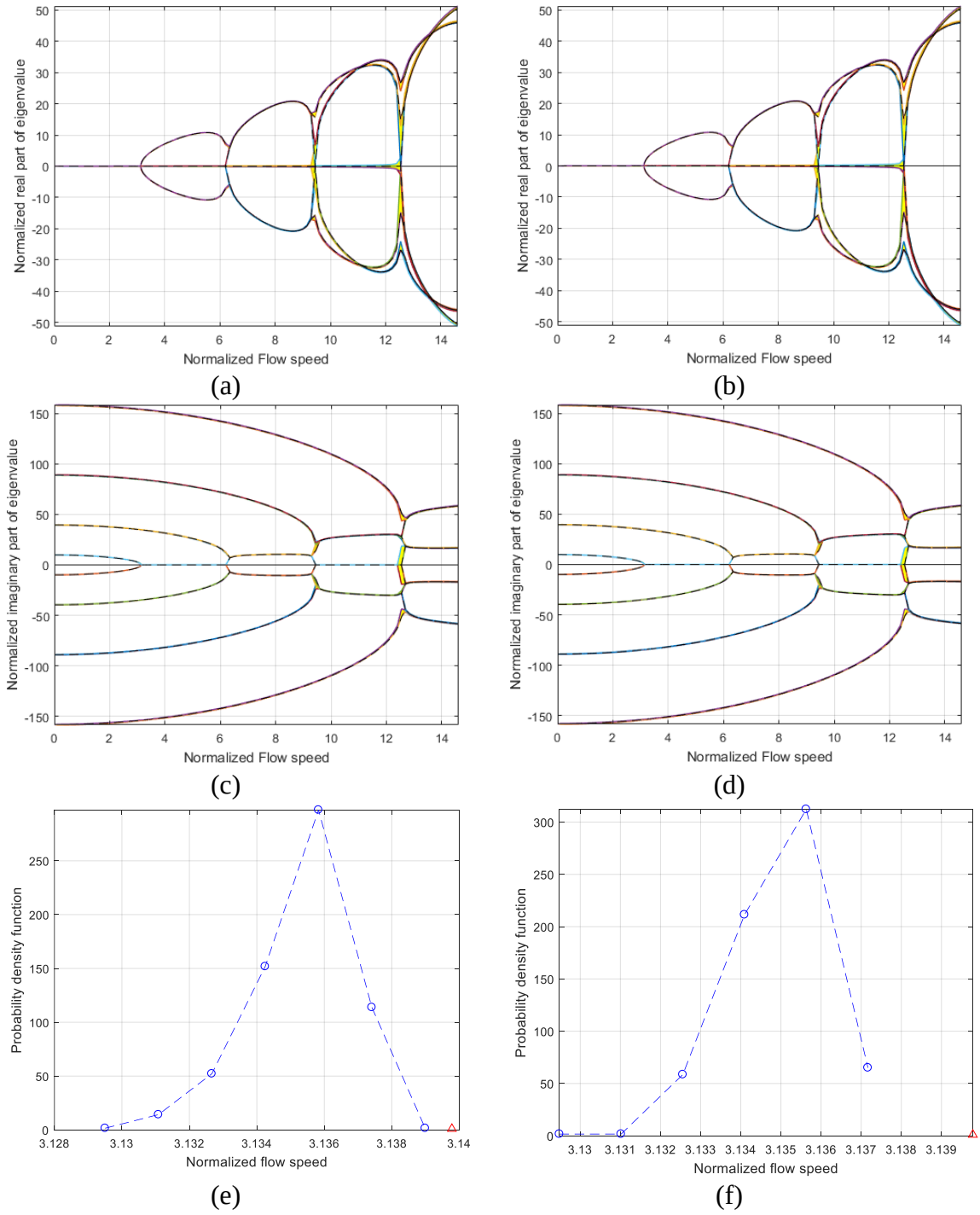

Figure 12. (a),(b) Normalized real part of eigenvalues vs. normalized flow speed; (c),(d) normalized imaginary part of eigenvalues vs. normalized flow speed; (e),(f) probability density function of divergence speed. Mean model shown as "--". (a),(c),(e) Gaussian and (b),(d),(f) uniform inner radius distribution for simply supported pipes - option 3

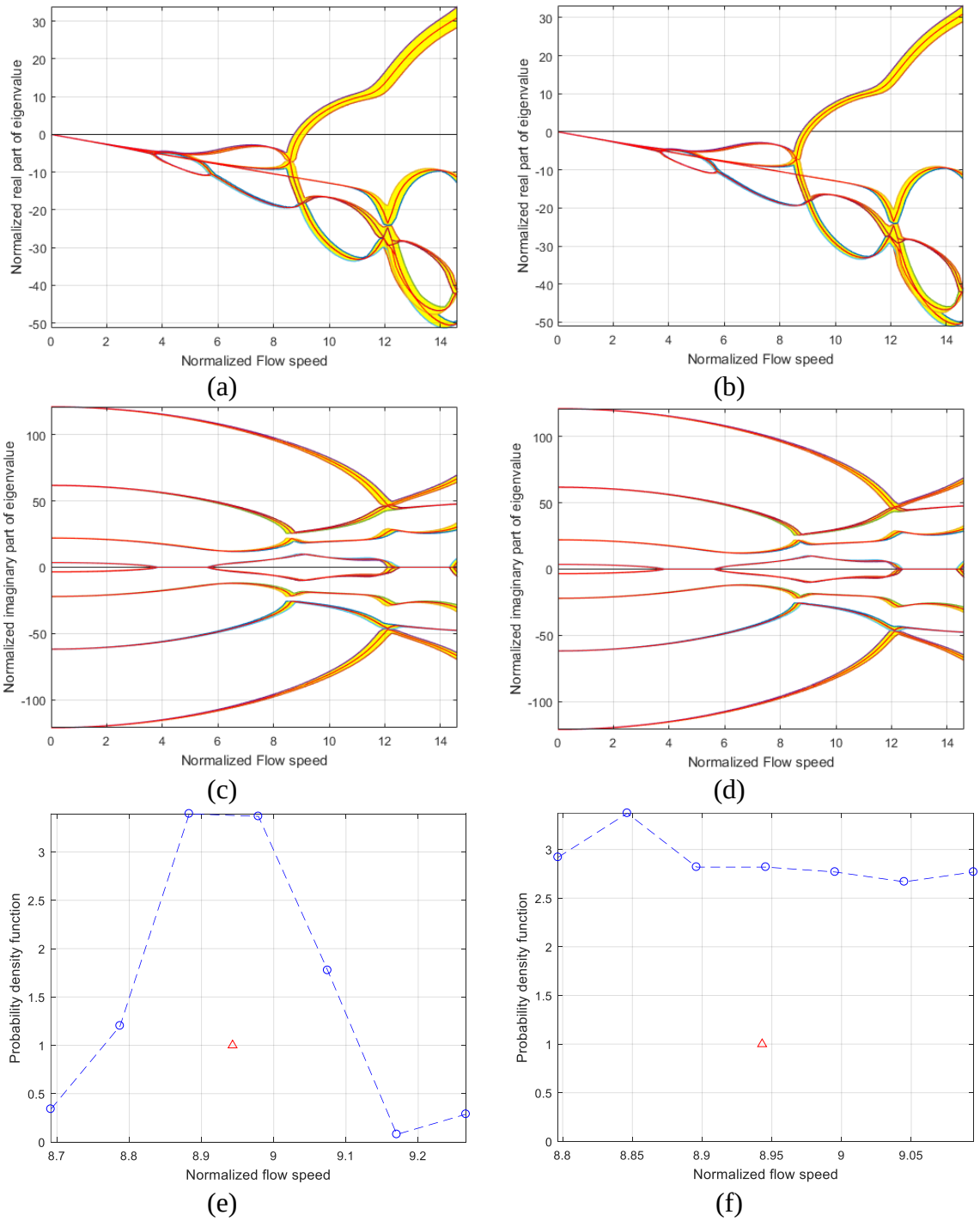

Figure 13. (a),(b) Normalized real part of eigenvalues vs. normalized flow speed; (c),(d) normalized imaginary part of eigenvalues vs. normalized flow speed; (e),(f) probability density function of divergence speed. Mean model shown as "--". (a),(c),(e) Gaussian and (b),(d),(f) uniform inner radius distribution for cantilevered pipes - option 1

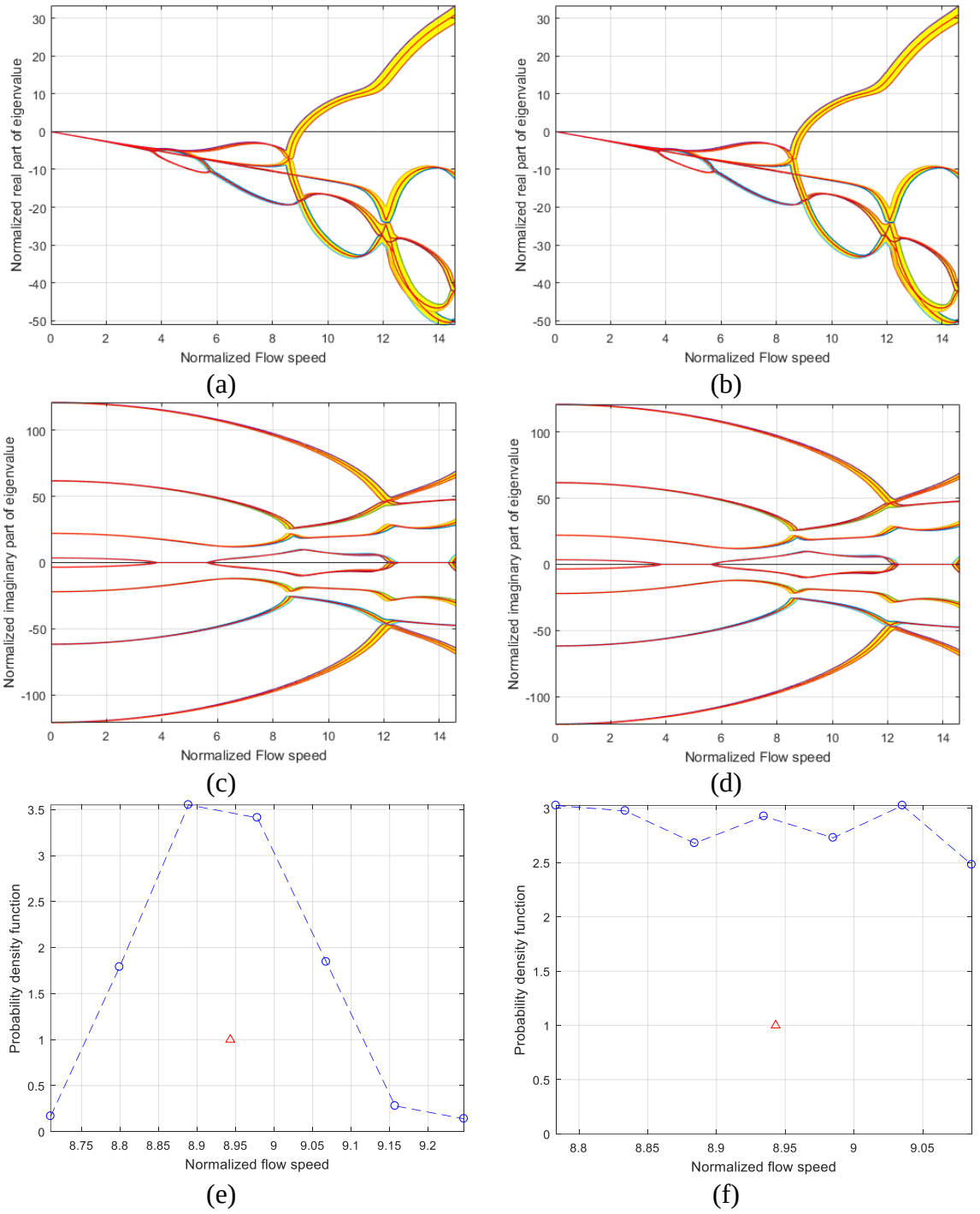

Figure 14. (a),(b) Normalized real part of eigenvalues vs. normalized flow speed; (c),(d) normalized imaginary part of eigenvalues vs. normalized flow speed; (e),(f) probability density function of divergence speed. Mean model shown as "--". (a),(c),(e) Gaussian and (b),(d),(f) uniform inner radius distribution for cantilevered pipes - option 2

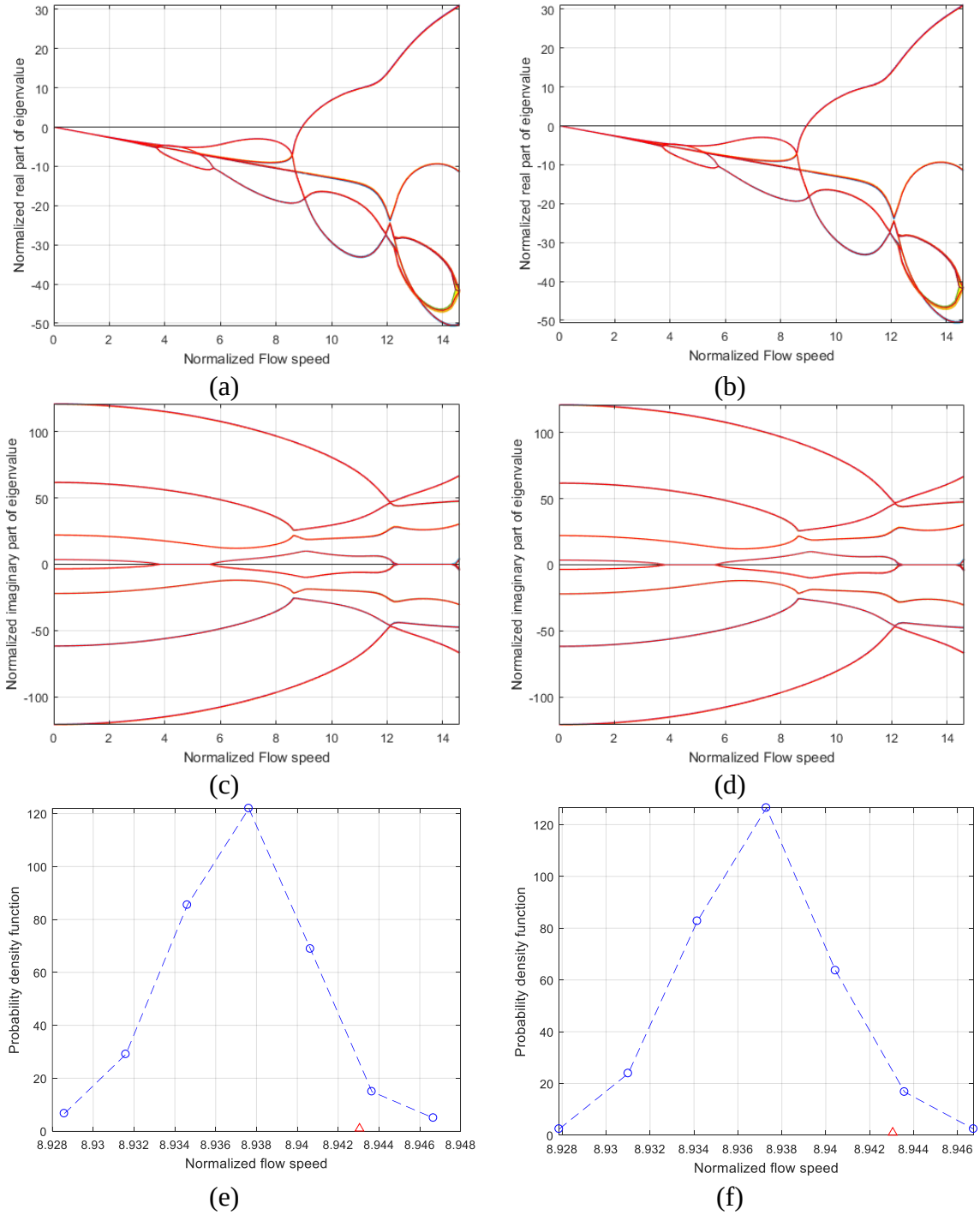

Figure 15. (a),(b) Normalized real part of eigenvalues vs. normalized flow speed; (c),(d) normalized imaginary part of eigenvalues vs. normalized flow speed; (e),(f) probability density function of divergence speed. Mean model shown as "--". (a),(c),(e) Gaussian and (b),(d),(f) uniform inner radius distribution for cantilevered pipes - option 3

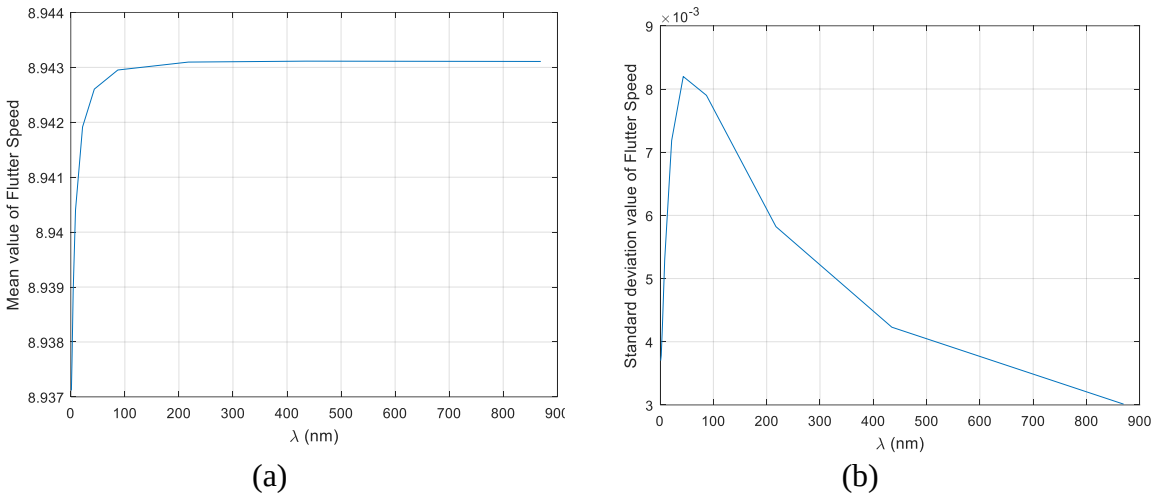

Figure 16. (a) Mean value and (b) standard deviation of flutter speed for randomly tapered cantilevered pipes as functions of the correlation length – option 3

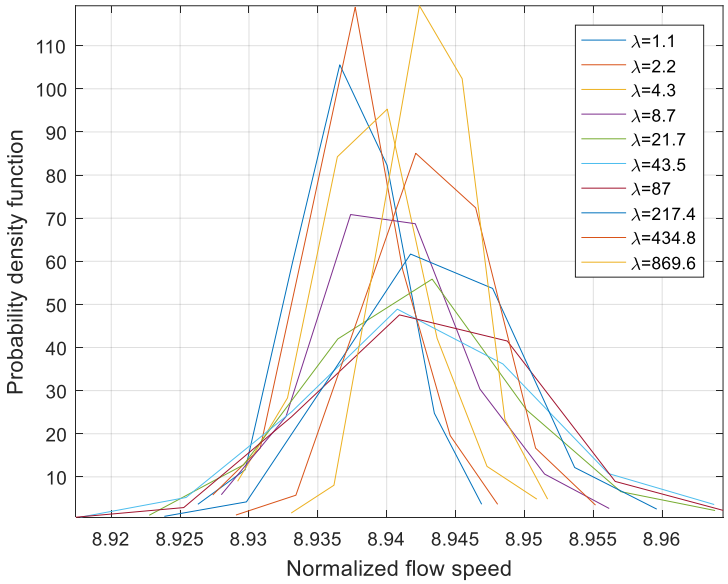

Figure 17. Probability distribution of flutter speed for randomly tapered cantilevered pipes as a functions of the correlation length-option 3

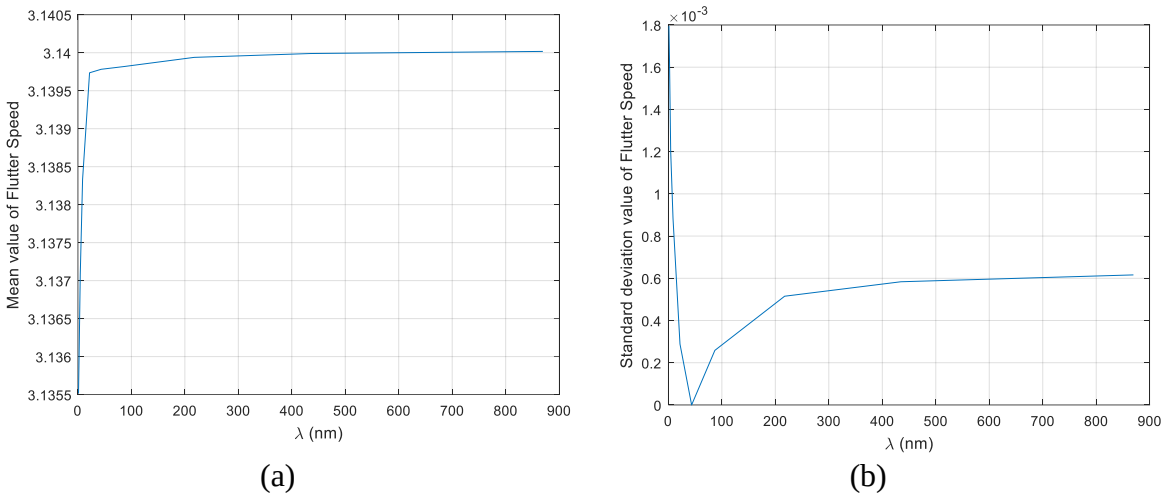

Figure 18. (a) Mean value and (b) standard deviation of divergence speed for randomly tapered simply supported pipes as functions of the correlation length – option 3

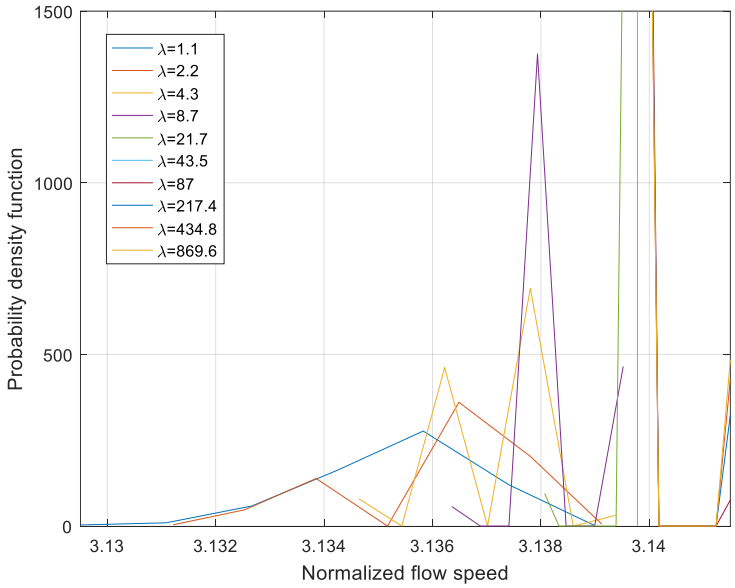

Figure 19. Probability distribution of divergence speed for randomly tapered simply supported pipes as a functions of the correlation length-option 3

CHAPTER FOUR

DEVELOPMENT OF A STOCHASTIC MODEL FOR STRAIGHT PIPES WITH VARYING CROSS SECTION

4.1 Overall Perspective

The discovery effort carried out in the previous chapters aimed at providing both qualitative and quantitative data to be used in developing, in this chapter, a more generic stochastic model of straight pipes conveying fluid. One of the challenges involved in constructing detailed stochastic models (as in the previous chapters) of uncertain structures, pipes here, is the need to completely characterize the uncertainty. For example, the inner radius must be specified as a stochastic process, that is, all of the joint probability density functions of its values at the finite element nodes must be known or imposed. The deviations in shape of the inner cross-section (not considered in Chapters 2 and 3) would also need to be defined, etc. Obtaining such data on a number of samples would represent a tremendously painstaking task and would be time consuming to implement. These issues motivate the construction of a more generic or global model of the uncertainty.

The approach selected here for the construction of such a model is the one successfully implemented in a series of structural dynamics problems (see [17] for a review), i.e.,

(i) develop a reduced order model (ROM) of the mean model, the straight pipe with constant cross-section here,

(ii) randomize the matrices involved in the ROM using the maximum entropy concepts [17,18] ensuring that all physical constraints on the random matrices are satisfied.

Section 4.2 describes the development of a reduced order modeling of the mean model and its properties while section 4.3 provides a brief overview of the maximum entropy approach. Next, section 4.4 presents the construction of the stochastic reduced order model which is then critically assessed in comparison with the results of Chapter 3 in section 4.5.

4.2 Mean Model Reduced Order Modeling

The mean model here describes a perfectly straight pipe with constant cross-section. Then, its governing equation is obtained from Eq. (2.3) with A_i constant, that is

$$\frac{\partial^2}{\partial x^2}\left[EI\,\frac{\partial^2 w}{\partial x^2}\right] + \rho_i A_i \left\{ \frac{\partial^2 w}{\partial t^2} + 2U_i\,\frac{\partial^2 w}{\partial x \partial t} + U_i^2\,\frac{\partial^2 w}{\partial x^2}\right\} + m\frac{\partial^2 w}{\partial t^2} = 0 \tag{4.1}$$

A ROM of this equation can be obtained by seeking a solution of the form

$$w(x,t) = \sum_{j=1}^{N} q_j(t)\,\varphi_j(x) \tag{4.2}$$

where $\varphi_j(x)$ are basis functions satisfying the geometric boundary conditions, $q_j(t)$ are the corresponding generalized coordinates, and N is the number of such terms. Then, proceeding in a Gakerkin format as in the finite element modeling, leads to the following set of ordinary differential equations for the generalized coordinates stacked in the vector $\underline{q}$

$$\left(\overline{M}_p + \overline{M}_f\right)\ddot{\underline{q}} + \overline{C}_f\,\dot{\underline{q}} + \left(\overline{K}_p + \overline{K}_f\right)\underline{q} = \underline{0} \tag{4.3}$$

where $\overline{M}_p$, $\overline{M}_f$, $\overline{C}_f$, $\overline{K}_p$, $\overline{K}_f$ are, respectively, the pipe and fluid-induced mass matrices, the fluid-induced damping matrix, and the pipe and fluid-induced stiffness matrices, the *rs* elements of which all are

$$\overline{M}_{p,rs} = \int_0^L \rho_p \, \varphi_r(x)\varphi_s(x)dx \;,\; \overline{M}_{f,rs} = \int_0^L \rho_f \, \varphi_r(x)\varphi_s(x)dx \qquad \text{(4.4a), (4.4b)}$$

$$\overline{C}_{f,rs} = \int_0^L \rho_f \, U \, \varphi_r(x)\frac{d\varphi_s}{dx}(x)dx = \left[\rho_f \, U \, \varphi_r \, \varphi_s \right]_0^L - \int_0^L \rho_f \, U \, \frac{d\varphi_r}{dx}(x)\varphi_s(x)dx \qquad (4.5)$$

and

$$\overline{K}_{f,rs} = \int_0^L \rho_f \, U^2 \, \varphi_r(x)\frac{d^2\varphi_s}{dx^2}dx = \left[\rho_f \, U^2 \, \varphi_r \, \frac{d\varphi_s}{dx} \right]_0^L - \int_0^L \rho_f \, U^2 \, \frac{d\varphi_r}{dx}(x)\frac{d\varphi_s}{dx}(x)dx$$

$$\overline{K}_{p,rs} = \int_0^L EI \, \frac{d^2\varphi_r}{dx^2}(x)\frac{d^2\varphi_s}{dx^2}(x)dx \qquad \text{(4.6a), (4.6b)}$$

An inspection of Eqs (4.4)-(4.6) provides a series of properties that hold independently of the boundary conditions. More specifically, the matrix $\overline{M}_p$ is symmetric, as $\overline{M}_{p,rs} = \overline{M}_{p,sr}$, but it is also positive definite since

$$\underline{z}^T \overline{M}_p \underline{z} = \sum_{r,s=1}^{N} \overline{M}_{p,rs} z_r z_s = \int_0^L \rho_p \left[\sum_{r=1}^{N} \varphi_r(x) z_r \right] \left[\sum_{s=1}^{N} \varphi_s(x) z_s \right] dx$$

$$= \int_0^L \rho_p \left[\sum_{r=1}^{N} \varphi_r(x) z_r \right]^2 dx \geq 0 \qquad (4.7)$$

for any vector $\underline{z}$ of components z_r. Following the same arguments, it is found that $\overline{M}_f$ and $\overline{K}_p$ are also symmetric and positive definite. In general, the matrices $\overline{C}_f$ and $\overline{K}_f$

do not have any particular property but they do when the pipe is simply supported. In that case, the boundary terms in Eq. (4.5) and (4.6) vanish and one observes that $\overline{C}_f$ is skew-symmetric, and $\overline{K}_f$ is symmetric and negative definite. In fact, these properties are critical to prove that the pipe will exhibit divergence as opposed to flutter, see Appendix A for a proof.

Moreover, one can construct a matrix that regroups them and which has similar property. To this end, note first that

$$E = \int_0^L \rho_f \left[\sum_{r=1}^{N} y_r \varphi_r(x) + z_r U \frac{d\varphi_s}{dx}(x) \right] \left[\sum_{s=1}^{N} y_s \varphi_s(x) + z_s U \frac{d\varphi_s}{dx}(x) \right] dx \tag{4.8}$$

is positive for any combination of values y_r and z_r as the integrand is always positive. Expanding the product of the two brackets, it is found that

$$E = \sum_{r,s=1}^{N} \left[\overline{M}_{f,rs}\, y_r\, y_s + 0.5\, \overline{C}_{f,rs}\, y_r\, z_s + 0.5\, \overline{C}_{f,sr}\, y_s\, z_r - \overline{K}_{f,rs}\, z_r\, z_s \right] \tag{4.9}$$

Since this expression should be positive for all values of y_r and z_r, the symmetric matrix $\overline{F}$ defined as

$$\overline{F} = \begin{bmatrix} \overline{M}_f & 0.5\overline{C}_f \\ 0.5\overline{C}_f^T & -\overline{K}_f \end{bmatrix} \tag{4.10}$$

4.3 Standard Nonparametric Modeling – Symmetric Positive Definite Matrices

The nonparametric modeling is a strategy for the stochastic modeling of matrices exhibiting particular properties. The original formulation of this method [18] focuses on symmetric positive definite matrices *A* for which it assumes that the mean $\overline{A}$ is known.

This limited information is not sufficient to uniquely define the joint probability density function of the elements of *A*, denoted as $p_A(a)$. Faced with this issue, Soize proposed in [18] that this joint probability density function be selected as the one that maximizes the entropy *S* given the available information. That is, $p_A(a)$ should maximize

$$S = -\int_{\Omega} p_A(a) \ln\, p_A(a) da \tag{4.11}$$

given that

Unit total probability: $$\int_{\Omega} p_A(a)\, da = 1 \tag{4.12}$$

Given mean: $$\int_{\Omega} a\; p_A(a)\, da = \overline{A} \tag{4.13}$$

Nonsingularity: $$\int_{\Omega} \ln[\det(a)] p_A(a)\, da = \nu \text{ finite} \tag{4.14}$$

where the domain of support Ω of the probability density function is then such that the matrix *A* is positive definite, or equivalently that it admits a Cholesky decomposition, i.e.,

$$\Omega = \left\{ a = \tilde{L}\tilde{L}^T ; \tilde{L}_{ij}, i, j = 1,..., n : \left[\tilde{L}_{ij} \in (-\infty, +\infty), i > j\right] \cap \left[\tilde{L}_{ii} \in [0, +\infty)\right] \right\} \tag{4.15}$$

The probability density function $p_A(a)$ maximizing *S* given the constraints of Eqs (4.12)-(4.14) can be derived by calculus of variation and is found to be

$$p_A(a) = \tilde{C}[\det(a)]^{\lambda - 1} \exp\left[-\operatorname{tr}\left(\tilde{\mu}^T a\right)\right] \tag{4.16}$$

where $\tilde{C}$ is the appropriate constant to satisfy the normalization condition, Eq. (4.12) and μ and λ are the Lagrange multipliers associated with the constraints of Eqs (4.13) and

(4.14), respectively. After a change of random variables, it is found that the matrices *A* of joint probability density function $p_A(a)$, Eq. (4.16), can be generated as

$$A = \bar{L}\, H\, H^T\, \bar{L}^T \tag{4.17}$$

Where $\bar{L}$ is any decomposition, e.g., Cholesky, of $\bar{A}$, i.e.,

$$\bar{A} = \bar{L}\, \bar{L}^T \tag{4.18}$$

Moreover, *H* is a lower triangular matrix such that (see also Fig. 18)

(1) its off-diagonal elements H_{il}, $i \neq l$, are normally distributed (Gaussian) random variables with standard deviation $\sigma = 1/\sqrt{2\mu}$, and

(2) its diagonal elements H_{ii} are obtained as $H_{ii} = \sqrt{Y_{ii}/\mu}$ where Y_{ii} is Gamma distributed with parameter $(p(i)-1)/2$ where

$$p(i) = n - i + 2\lambda_0 - 1 \text{ and } \quad \mu = (n + 2\lambda_0 - 1)/2 \tag{4.19}$$

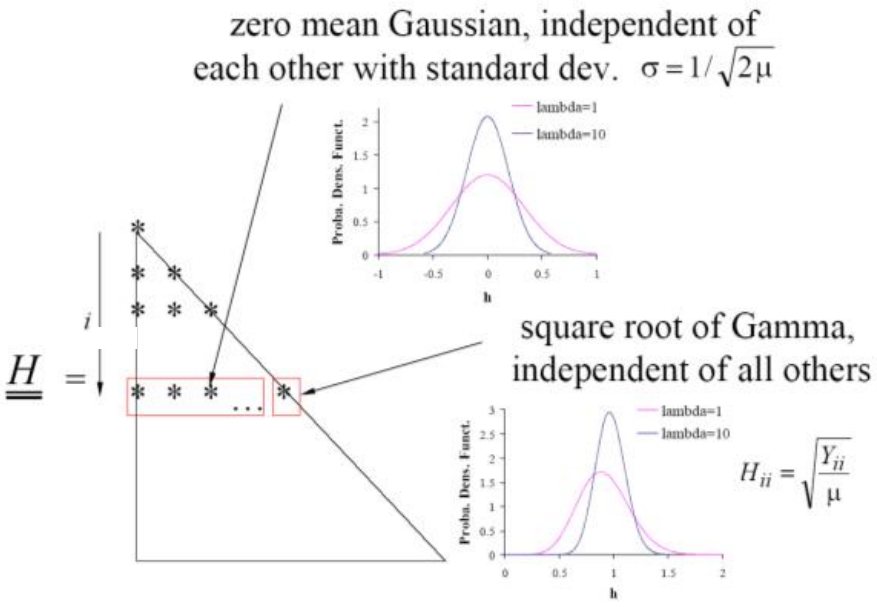

Figure 20. Structure of the random *H* matrices with *n* = 8, *i* =2, and λ_0 =1 and 10.

In the above equations, *n* is the size of the matrices and the parameter $\lambda_0 > 0$ is the free parameter of the statistical distribution of the random matrices *A*. An alternative parametrization is through the dispersion parameter δ defined as

$$\delta^2 = \frac{n+1}{n+2\lambda_0 - 1} \tag{4.20}$$

4.4 Stochastic ROM Construction

The first step in formulating a global modeling of uncertain pipe is to recognize that proceeding with the assumed representation of Eq. (4.2) in Eq. (2.3) would give a set of equations similar to Eq. (4.3) but with different matrices which would all involve the variations of the pipe's inner geometry in different manner. This observation would suggest that M_p, M_f, K_p, K_f and C_f should all be randomized together to model uncertainty in the internal cross-section properties. Of course, separate uncertainty on the density of the pipe, its outer diameter, Young's modulus, etc. would also come in inducing further uncertainty on the pipe's own matrices M_p and K_p and decreasing the dependence between the elements of these matrices and those of the fluid-induced ones. On this basis, it is suggested here that M_p and K_p can be modeled independently of the remaining three matrices M_f, C_f, and K_f which however ought to be modeled together since they originate from the same source, the fluid flow, and involve at least one common uncertain factor, i.e., the fluid mass per length which depends on the inner cross-section area. In considering the modeling of K_f, it should further be recognized that this matrix would be the only one affected by the exit flow velocity $U_i(L)$ since this

variable appears only in a stiffness term in Eq. (2.3) (i.e., a term without time derivative). Moreover, that term is the largest stiffness one in the case of small taper; it is in fact the only one present without taper. Finally, $U_i(L)$ is seen to scale this term. In summary, $U_i(L)$ provides a near scaling of the pipe stiffness when its taper is small.

The need for a combined modeling of the flow-induced matrices was also stated in [16]. The authors argued additionally that the fluid-induced mass matrix could be lumped with the pipe's own since they exhibit a similar symmetry. That left the fluid-induced stiffness and damping matrices which were ingeniously combined into a complex impedance modeled according to the extension of the nonparametric method applicable to general matrices [17].

A different perspective in generating the random matrices M_f, C_f and K_f is adopted here based on the expectation that, for appropriately small uncertainty levels,

(i) the uncertain pipes exhibit the same type of instability, flutter or divergence, as the mean model, and

(ii) the pipes becomes unstable at flow speeds close to the critical speed of the mean model.

The property (i) is in fact much more stringent that could be imagined at first especially for the case of simply supported pipes. Since the perfectly straight simply supported pipe diverges, the real parts of all its eigenvalues are exactly zero until divergence takes place. The condition (i) then requires that a similar result be obtained for the uncertain system. This condition is however not achieved by any arbitrary small variations of M_f, C_f, and K_f which, on the contrary, typically lead to the occurrence of complex eigenvalues

with small negative real part (indicative of flutter) at much lower speeds than the divergence speed, sometimes even as $U \rightarrow 0$ which is clearly unphysical (and in opposition of requirement (ii)).

The above observations suggests here that it is necessary to impose a particular structure to the random matrices M_f, C_f, and K_f of the uncertain pipes. In the absence of clearer information, it will be *assumed* here that these matrices satisfy the same properties as the perfectly straight simply supported pipe, that is

(a) M_f is symmetric positive definite, C_f is skew-symmetric, and K_f is symmetric and negative definite.

Then, it is guaranteed from Appendix A that divergence will occur. Moreover, for small enough uncertainty level, it will be expected that

(b) the matrix F obtained as in Eq. (4.10) with the matrices M_f, C_f, and K_f is positive definite.

Then, the uncertain simply supported pipes diverge and any early onset of flutter is avoided. The conditions (a) and (b) will be enforced by expressing M_f, C_f and K_f as

$$M_f = P^T \overline{M}_f P \qquad C_f = P^T \overline{C}_f P \quad K_f = P^T \overline{K}_f P \qquad \text{(4.21a), (4.21b), (4.21c)}$$

where P is a NxN random matrix to be selected. It is readily shown that these relations guarantee the needed symmetry/skew symmetry and negative definiteness properties of M_f, C_f, and K_f. They do also imply the condition (b) since

$$F = \begin{bmatrix} M_f & 0.5C_f \\ 0.5C_f^T & -K_f \end{bmatrix} = \begin{bmatrix} P^T & 0 \\ 0 & P^T \end{bmatrix} \begin{bmatrix} \overline{M}_f & 0.5\overline{C}_f \\ 0.5\overline{C}_f^T & -\overline{K}_f \end{bmatrix} \begin{bmatrix} P & 0 \\ 0 & P \end{bmatrix} = Q^T \overline{F} Q \qquad (4.22)$$

where

$$Q = \begin{bmatrix} P & 0 \\ 0 & P \end{bmatrix} \tag{4.23}$$

While the above discussion strictly holds only for simply supported pipes, it is desirable that the construction of the stochastic reduced order model be independent of the boundary conditions. Thus, Eqs (4.21) will also be applied for all boundary conditions, e.g., also for cantilevered pipes.

It remains finally to address the explicit dependence of K_f on the exit flow velocity $U_i(L)$, i.e., the dependence of this matrix on a single random variable modeling the jet effect at the outlet. As discussed above, this speed effectively scales the stiffness matrix K_f. It is thus proposed here to modify Eq. (4.21c) to read

$$K_f = R\, P^T \overline{K}_f\, P \tag{4.24}$$

where the positive random variable *R* is introduced to model the effects of the exit flow velocity $U_i(L)$.

In this light, the present model, Eqs (4.21a), (4.21b) and (4.24) is a combined parametric-non parametric model as first investigated in [34], see also [17] and [35] for a somewhat similar example.

To complete the stochastic ROM construction, it then remains to specify the distribution of the random variable *R* and of the random matrix *P*. It is proposed here to rely on the maximum entropy approach [17]. More specifically, the application of this methodology, see Eqs (4.17)-(4.18), to the mass matrix M_f alone would lead to

$$M_f = \bar{L}\, H_N\, H_N{}^T\, \bar{L}^T \qquad \text{where} \qquad \overline{M}_f = \bar{L}\, \bar{L}^T \tag{4.25}$$

with H_N a *N*x*N* lower triangular matrix as in section 4.3, see also Fig. 18. The single hyperparameter of this distribution is the overall measure of deviation, δ_N. Equating the random mass matrices M_f of Eqs (4.21a) and (4.25) yields a desired expression for *P*, i.e.,

$$P = \bar{L}^{-T}\, H_N{}^T\, \bar{L}^T \tag{4.26}$$

The modeling of the random variable R could be achieved in different ways. One approach would be to represent this variable in a polynomial chaos format, e.g., see [34,35]. A simpler approach is adopted here on the basis of the maximum entropy principle. Specifically, R is recognized as a 1x1 positive definite random matrix leading directly to its modeling as $R = H_1^2$ where H_1 is similar to H_N but with a matrix size of 1 and appropriate dispersion δ_1.

4.5 Mean Model ROM Validation

The first step in the development of the stochastic ROM described in the previous section is the construction of the deterministic ROM of the mean model. It was achieved from the finite element model to emulate the continuum formulation of Eqs (4.2) – (4.6). Specifically, the basis vectors $\underline{\varphi}_j(x)$ were selected as the linear modes of the pipe without flow which are obtained from the eigenvalue problem Eq. (1.3) or

$$\overline{K}_p^{FE}\, \underline{\varphi} = \left(-\lambda^2\right) \overline{M}_p^{FE}\, \underline{\varphi} \tag{4.27}$$

where $\overline{M}_p^{FE}$ and $\overline{K}_p^{FE}$ are the structural mass and stiffness matrices of the finite element model as given in chapter 2.

Then consistently with Eq. (4.2) the solution of Eq. (2.25) was sought in the form

$$\underline{w} = \sum_{j=1}^{N} q_j \underline{\varphi}_j = \Phi \underline{q} \tag{4.28}$$

where Φ is the matrix whose columns are the linear modes $\underline{\varphi}_j$. Then, the ROM mass, damping and stiffness matrices of the mean model are

$$\overline{M}_p = \Phi^T \overline{M}_p^{FE} \Phi \qquad \overline{M}_f = \Phi^T \overline{M}_f^{FE} \Phi \qquad \overline{C}_f = \Phi^T \overline{C}_f^{FE} \Phi$$

$$\overline{K}_p = \Phi^T \overline{K}_p^{FE} \Phi \qquad \overline{K}_f = \Phi^T \overline{K}_f^{FE} \Phi \tag{4.29}$$

where $\overline{M}_f^{FE}$, $\overline{C}_f^{FE}$, $\overline{K}_f^{FE}$ are the fluid induced mass, damping and stiffness matrices of the finite element model as given in chapter 2.

The ROM of the mean model, straight uniform pipe, was achieved using the first 6 linear modes in the simply supported case and the first 8 modes in the cantilevered case.

Shown in Fig. 19 and 20 are comparisons of the real and imaginary parts of the eigenvalues obtained for the simply supported and cantilevered uniform pipes by the FE method and the above ROM. Clearly the matching is excellent and the ROM can be used instead of the FE model to predict the behaviour of the uniform pipe. It remains to assess whether the ROM is appropriate for tapered pipes as well. To this end, the comparison of Fig. 20 was reconducted but for a uniformly tapered pipe with taper angle of 1.8 degree. Then, shown in Fig. 21 is a comparison of the real and imaginary parts of the eigenvalues

obtained by the ROM and the finite element model. The excellent match between these sets of results confirm the validity of the ROM basis for the present analysis.

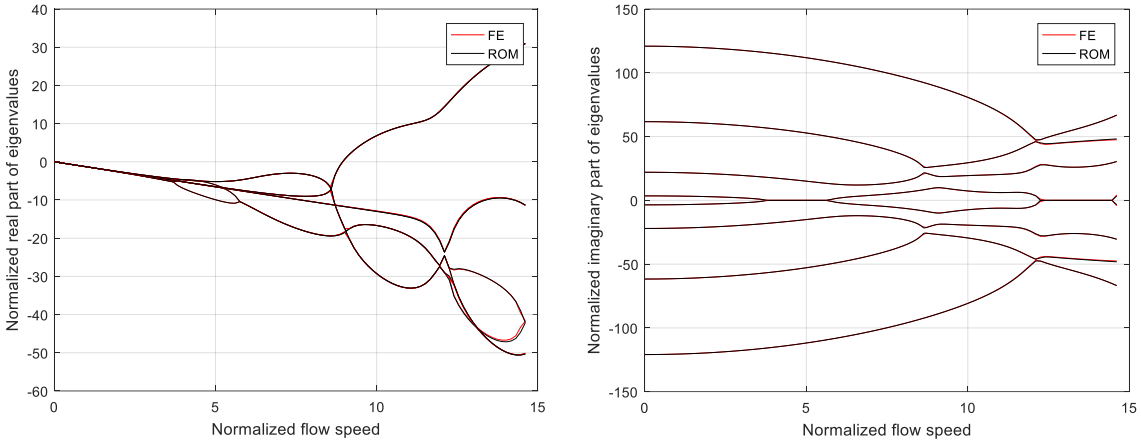

(a) (b)

Figure 21. Comparison of (a) normalized real part of eigenvalues vs normalized flow speed (b) normalized imaginary part of eigenvalues vs. normalized flow speed; finite element code and ROM for cantilevered pipe with uniform cross section

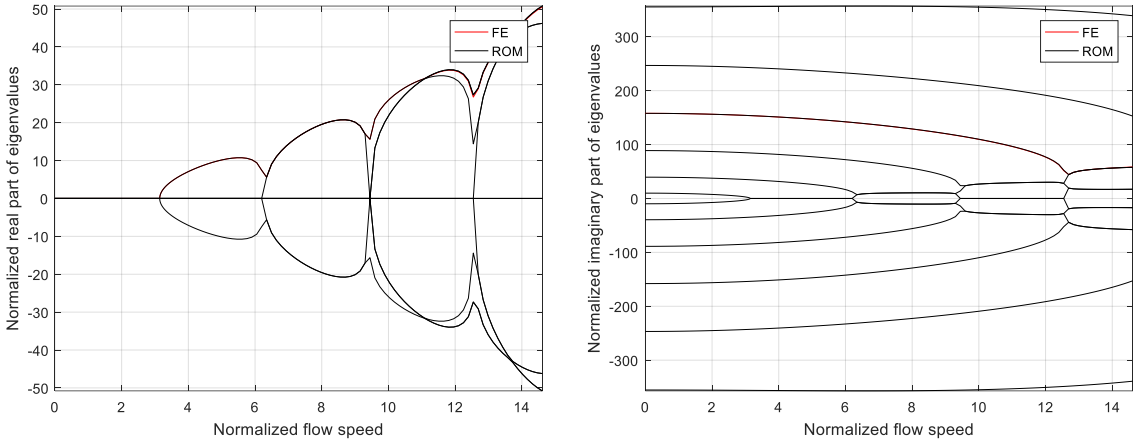

(a) (b)

Figure 22. Comparison of (a) normalized real part of eigenvalues vs normalized flow speed (b) normalized imaginary part of eigenvalues vs. normalized flow speed; finite element code and ROM for simply supported pipe with uniform cross section

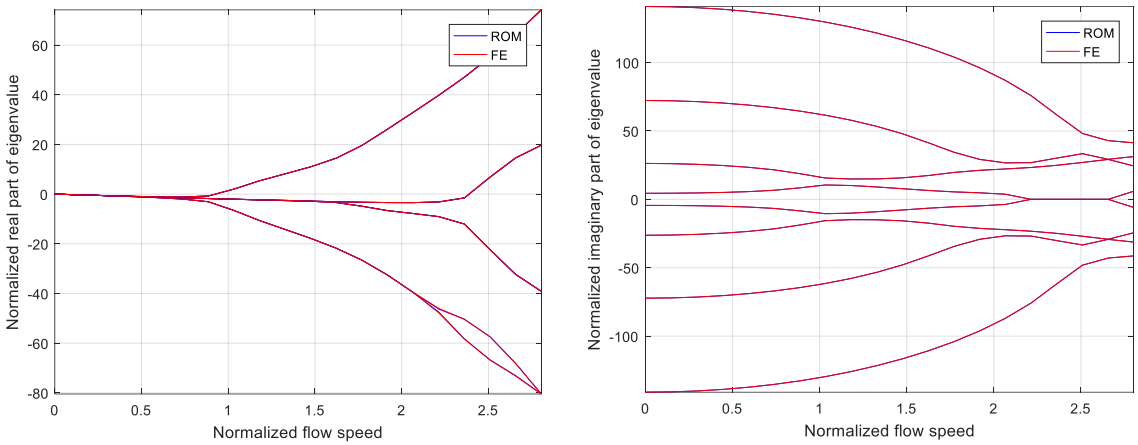

Figure 23. Comparison of (a) normalized real part of eigenvalues vs. normalized flow speed (b) normalized imaginary part of eigenvalues vs. normalized flow speed; finite element code and ROM for cantilevered pipe with taper angle of 1.8 degree

4.6 Stochastic ROM Assessment

To assess the potential of the stochastic ROM to match the physical behaviour of the randomly tapered pipes discussed in Chapter 3, the dispersion parameters δ_N and δ_1 were selected so that the standard deviations of the flutter and divergence speed obtained by the stochastic ROM match their counterparts for options 1 (when $\delta_N = 0;\ \delta_1 \neq 0$) and 3 (when $\delta_N \neq 0;\ \delta_1 = 0$). The stochastic ROM thus calibrated was then applied to both simply supported and cantilevered pipes in options 1, 2, and 3 and its eigenvalues, real and imaginary parts, were tracked as a function of the flow speed *U*. Moreover, the probability density function of the critical speed, flutter for the cantilever configuration and divergence for the simply supported one, was estimated as well. These results were then compared to their counterparts of Chapter 3.

Consider the simply supported configuration first. Calibrating the dispersion parameters δ_N and δ_1 from the standard deviation of the divergence speed obtained under the truncated Gaussian distribution of inner radii for options 1 and 3, it is found that $\delta_N = 0$ and $\delta_1 = 0.0294$ for option 1 and $\delta_N = 0.0021$ and $\delta_1 = 0$ for option 3. Proceeding next with these values, shown in Figs 22, 24, 26 are the corresponding plots of the real and imaginary parts of the eigenvalues for all three options. Comparing these with their counterparts of Chapter 3, i.e., Figs 10-12, it is seen that a very close match of the uncertainty bands is obtained. The comparison of the probability density functions of the divergence speed is shown on Figs 23, 25, 27. The stochastic ROM results clearly provide a very good agreement of the general shape of the probability density functions obtained with the truncated Gaussian and uniform inner radii. For options 1 and 3, the match is close with the Gaussian results, further with the uniform ones, as expected from the similarity of the Gaussian and Gamma distributions. For option 2, all three distributions are close but note that the divergence speeds exhibit a slight mean shift which is different in all three models.

Proceeding next with the cantilevered configuration, shown in Figs 28, 30, 32 are the plots of the real and imaginary parts of the eigenvalues for all three options which again match very closely their counterparts of Chapter 3, Figs 13-15. These results were obtained with the values $\delta_N = 0$ and $\delta_1 = 0.015$ for option 1 and $\delta_N = 0.00025$ and $\delta_1 = 0$ option 3, that yield equal standard deviations of the flutter speed of the random taper finite element code (with truncated Gaussian inner radii) and of the stochastic ROM for options 1 and 3. Comparing the probability density functions of the flutter speed, see Figs

29, 31, 33, lead here to the same observations as for the simply supported configuration. Note that Figs 27 and 33 show the deviations of the divergence and flutter speeds from their mean value to better demonstrate the similarities. Finally, it is observed from the above discussion that the parameter δ_1 is very closely equal to twice the coefficient of variation of the inner radius. This is in fact fully expected as, by conservation of the volumetric flow rate, $U(L)$ is inversely proportional to the inner radius and thus the coefficient of variation of the random variable *R* which models it (and is equal to δ_1) should be close to twice the corresponding value for the inner radius.

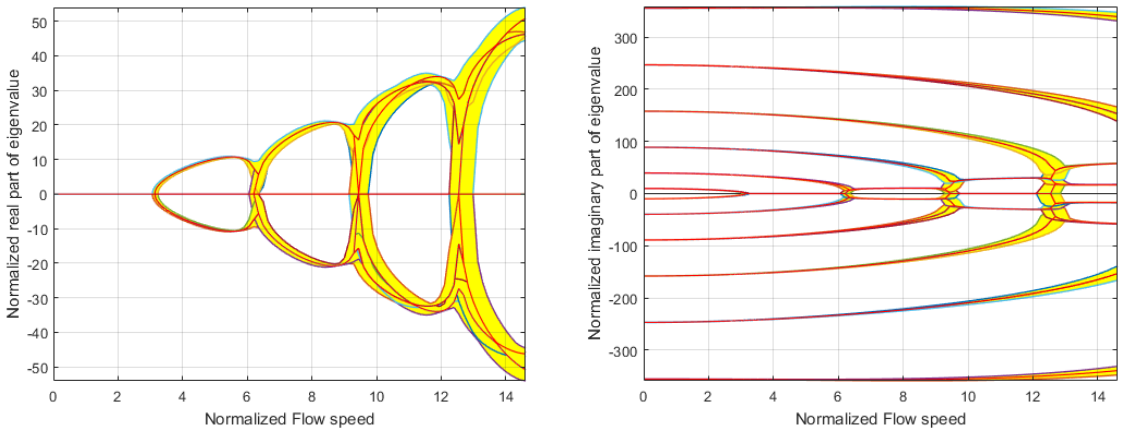

(a) (b)

Figure 24. (a) Normalized real part of eigenvalues vs. normalized flow speed; (b) normalized imaginary part of eigenvalues vs. normalized flow speed - stochastic ROM of simply supported pipe - option 1

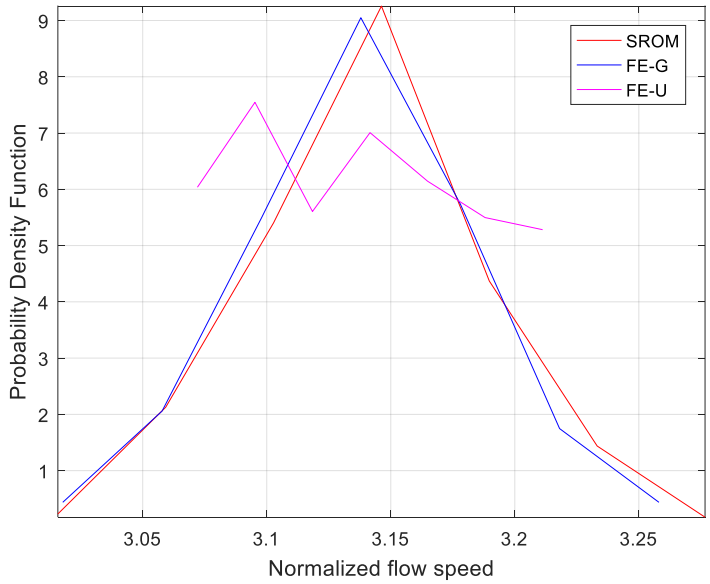

Figure 25. Probability density functions of divergence speed; tapered finite element code with Gaussian and uniform distribution and stochastic ROM; simply supported pipes - option 1

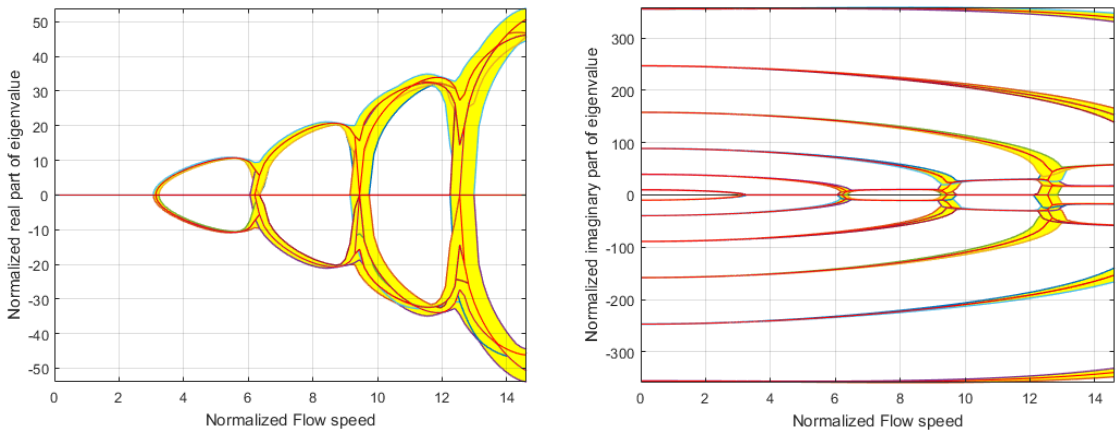

(a) (b)

Figure 26. (a) Normalized real part of eigenvalues vs. normalized flow speed; (b) normalized imaginary part of eigenvalues vs. normalized flow speed - stochastic ROM of simply supported pipe - option 2

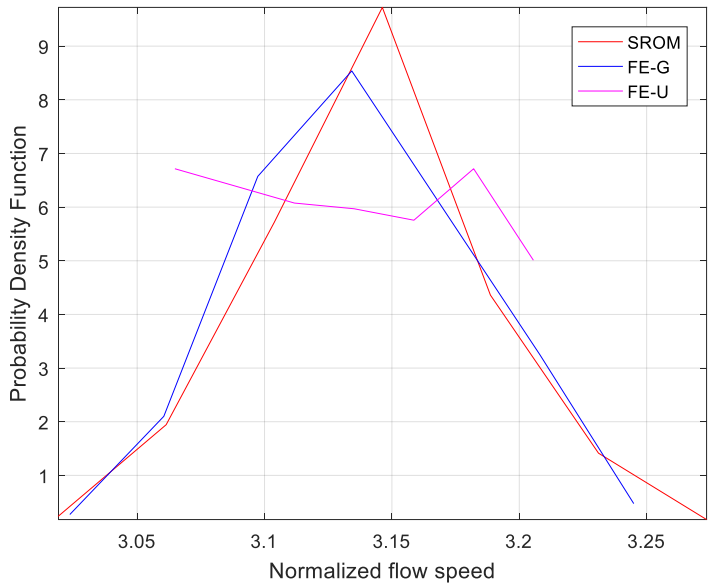

Figure 27. Probability density functions of divergence speed; tapered finite element code with Gaussian and uniform distribution and stochastic ROM; simply supported pipes - option 2

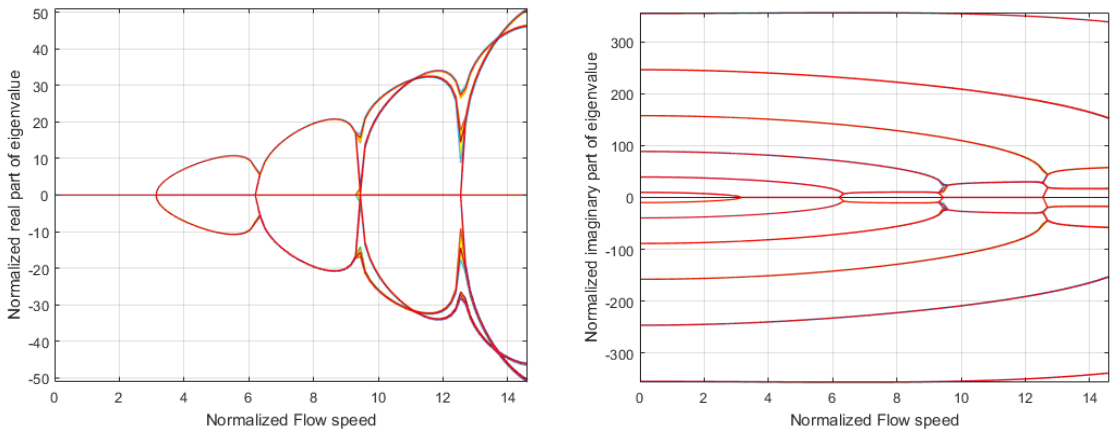

(a) (b)

Figure 28. (a) Normalized real part of eigenvalues vs. normalized flow speed; (b) normalized imaginary part of eigenvalues vs. normalized flow speed – stochastic ROM of simply supported pipe - option 3

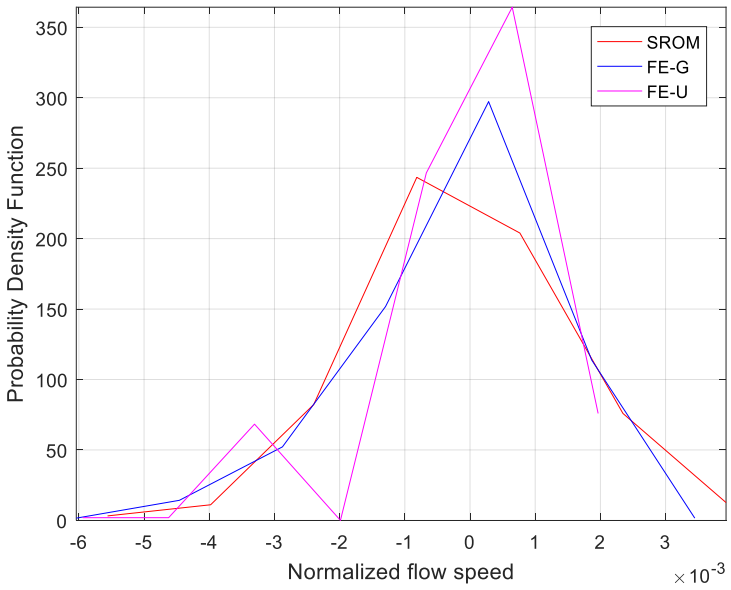

Figure 29. Probability density functions of divergence speed deviations; tapered finite element code with Gaussian and uniform distribution and stochastic ROM; simply supported pipes - option 3

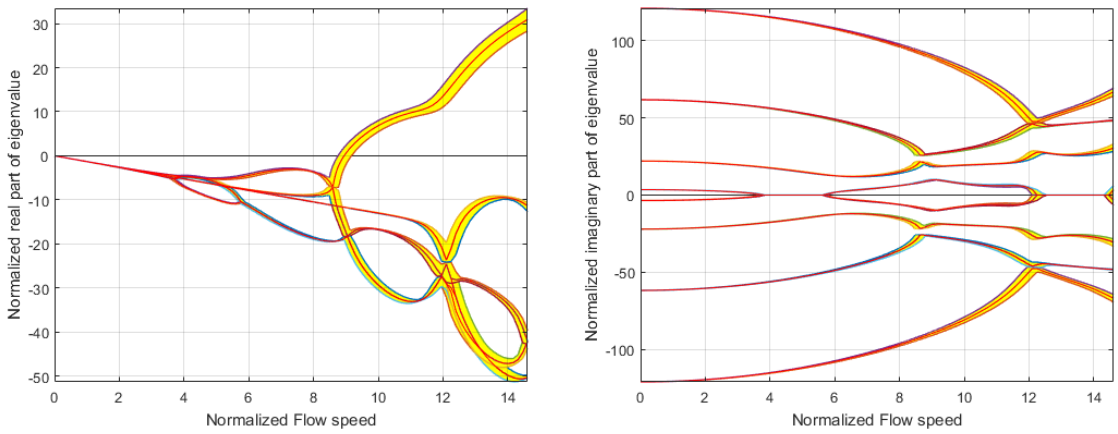

(a) (b)

Figure 30. (a) Normalized real part of eigenvalues vs. normalized flow speed; (b) normalized imaginary part of eigenvalues vs. normalized flow speed - stochastic ROM of cantilevered pipe - option 1

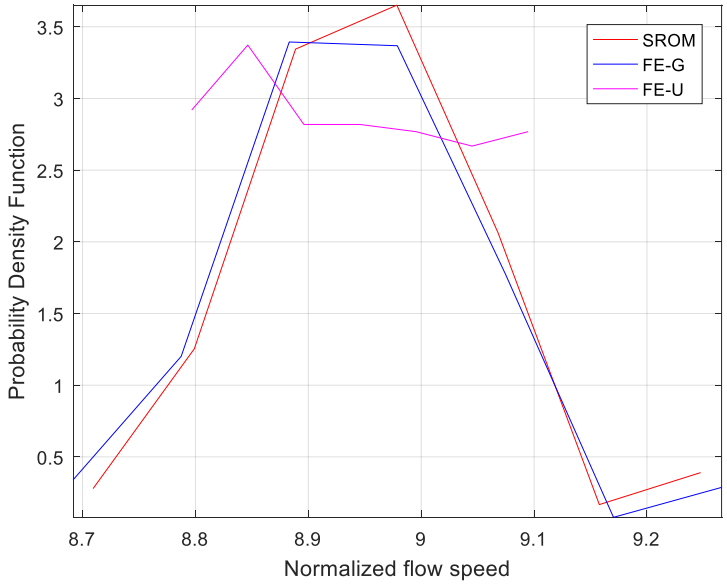

Figure 31. Probability density functions of flutter speed; tapered finite element code with Gaussian and uniform distribution and stochastic ROM; cantilevered pipes - option 1

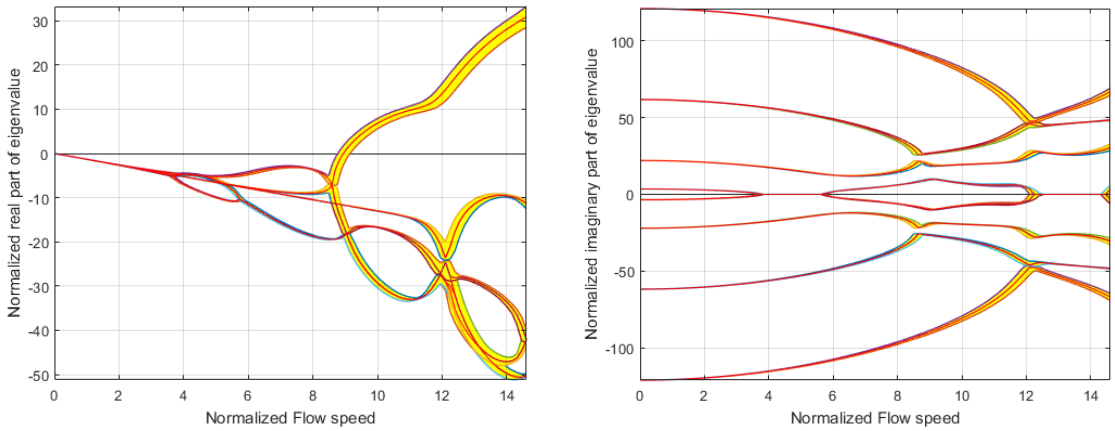

(a) (b)

Figure 32. (a) Normalized real part of eigenvalues vs. normalized flow speed; (b) normalized imaginary part of eigenvalues vs. normalized flow speed - stochastic ROM of cantilevered pipe - option 2

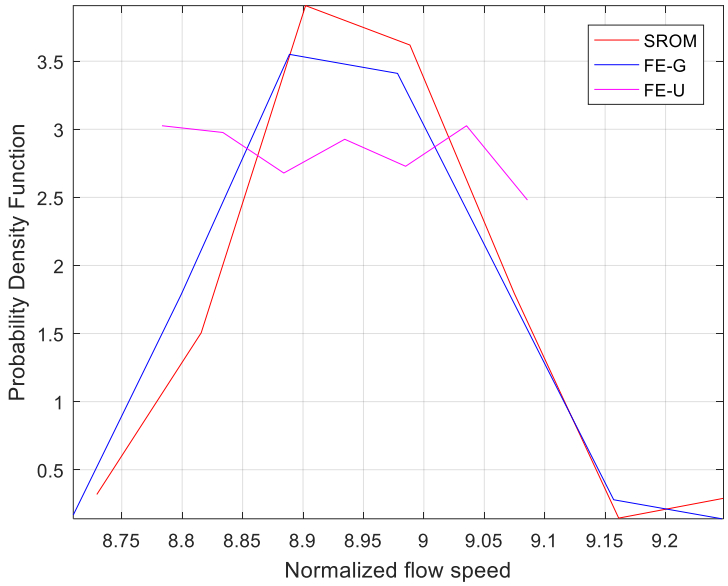

Figure 33. Probability density functions of flutter speed; tapered finite element code with Gaussian and uniform distribution and stochastic ROM; cantilevered pipes - option 2

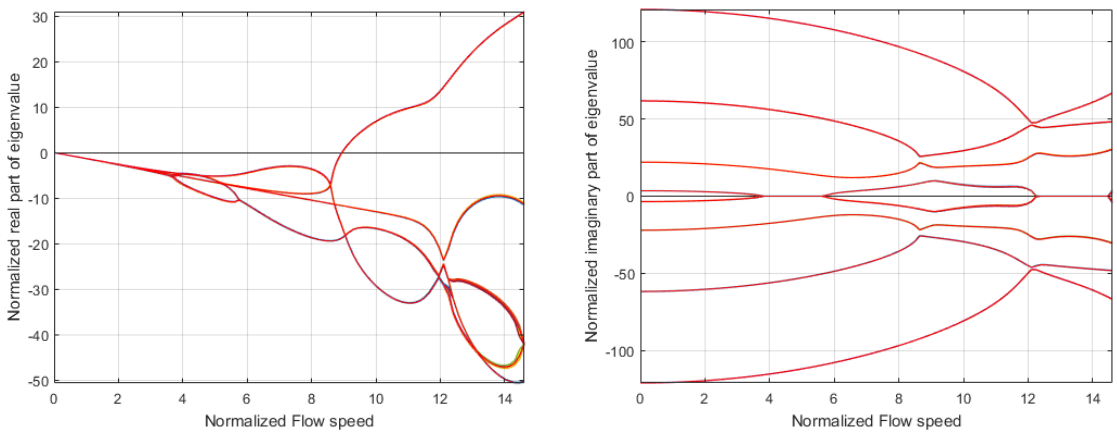

(a) (b)

Figure 34. (a) Normalized real part of eigenvalues vs. normalized flow speed; (b) normalized imaginary part of eigenvalues vs. normalized flow speed – stochastic ROM of cantilevered pipe - option 3

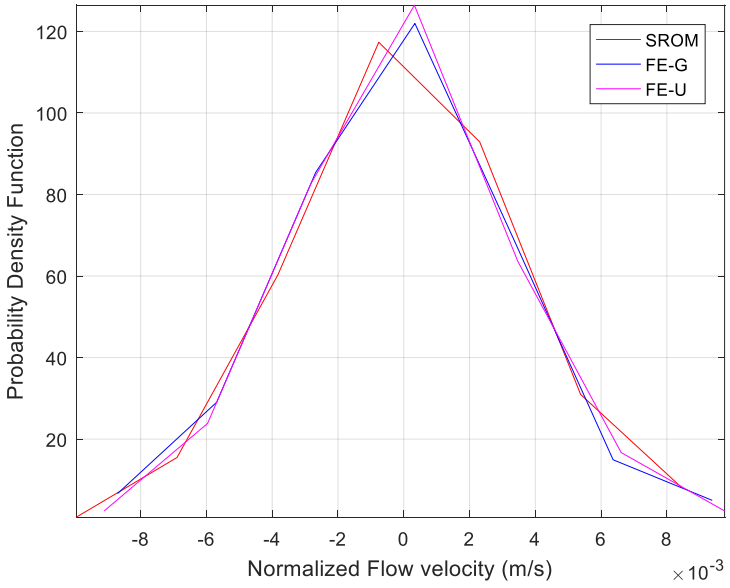

Figure 35. Probability density functions of flutter speed deviations; tapered finite element code with Gaussian and uniform distribution and stochastic ROM; cantilevered pipes - option 3

CHAPTER FIVE

EFFECTS OF PIPE CURVATURE AND FULL STOCHASTIC REDUCED ORDER MODEL

The previous chapters have focused extensively on the variations of inner radius/cross-section but the curvature of a pipe is also known to significantly affect its dynamic behavior/response. In his book [1], Paidoussis dedicates one chapter to the study of curved pipes, circular arcs of finite curvature in particular, which are analyzed in a related curvilinear frame. A key discussion item in that chapter is that the fluid flow in the curved pipe generates on it a steady loading which induces both static stress and displacement fields which in turn affect the pipe geometry and dynamic response. The stress fields includes in particular an axial preload which is known to potentially affect the pipe transverse behavior.

Closer to the present focus are the investigations of [14,15] which consider slightly curved beams and investigate briefly the linear response, e.g., eigenvalue vs. flow speed, but much more deeply the nonlinear geometric response past divergence (which is not part of the present investigation). It is observed that their formulation is in the Cartesian frame that would be used for the straight pipe but with the displacement measured from the statically deformed pipe. This relative positioning is not convenient in the current framework given the randomness of the undeformed pipe geometry and thus a revisit of the formulation is warranted. More specifically, the two key questions to address/quantify are (a) the expression of the flow induced forces and (b) the effect of a potential axial force in the pipe. The ensuing discussion will involve the following three transverse

positions of the beam at axial location x and time t: $w_0(x)$ the position corresponding to the undeformed pipe (no flow), $w(x,t)$ the elastic transverse deflection, and $w_t(x,t) = w_0(x) + w(x,t)$ the total transverse position.

With regard to the flow induced forces, proceeding as in the case of a straight pipe, e.g., see [1], it is found that they are expressed as

$$\begin{aligned} F_{flow} &= -\rho_i A_i \left\{ \frac{\partial^2 w_t}{\partial t^2} + 2U_i \frac{\partial^2 w_t}{\partial x \partial t} + U_i^2 \frac{\partial^2 w_t}{\partial x^2} \right\} \\ &= -\rho_i A_i \left\{ \frac{\partial^2 w}{\partial t^2} + 2U_i \frac{\partial^2 w}{\partial x \partial t} + U_i^2 \frac{\partial^2 w}{\partial x^2} + U_i^2 \frac{\partial^2 w_0}{\partial x^2} \right\} \end{aligned} \tag{5.1}$$

as long as second order terms in w_t can be neglected.

Consider next the magnitude and effects of the axial preload $N(x,t)$. Neglecting the effects of the time varying deflection $w(x,t)$ (as to remain in a linear framework), the flow induced forces generating the axial preload are, from Eq. (5.1), $F_{flow}^{(0)} = -\rho_i A_i U_i^2 \frac{d^2 w_0}{dx^2}$. Then, it is concluded that the axial preload N will only depend on position (not time) and that its magnitude will be of order $F_{flow}^{(0)} \frac{dw_0}{dx}$, i.e., proportional to U_i^2 and an order higher in the curvature than $F_{flow}^{(0)}$. Moreover, its effects on the pipe response will be to modify the stiffness as is seen for example in the case of a straight pipe where it induces the term $-\frac{\partial}{\partial x}\left[N \frac{\partial w}{\partial x} \right]$. This discussion demonstrates that a small undeformed curvature of the pipe will induce a change in the effective stiffness K_f

. Thus, the uncertain effects of a preload generated by a random curvature can be absorbed in the randomization of K_f proposed in Chapter 4. It may still be argued whether this effect should be included or not in the model as it is a second order effect in the small curvature as shown above.

It should finally be recognized that the curvature of the pipes induces a natural coupling between the transverse and axial deflections so that the ROM should be extended to include the latter motions. However, following standard practice, it is expected that the natural frequencies of axial motions are much higher than their transverse counterparts so that a static condensation of the former ones on the latter can be accomplished. This process effectively reduces the modeling to only the transverse motions.

Then, proceeding with an expansion of the displacement field $w(x,t)$ as in Eq. (4.2) and expressing similarly $w_0(x)$, i.e.

$$w_0(x) = \sum_{j=1}^{N} q_j^{(0)} \varphi_j(x) \tag{5.2}$$

it is found that the linear ROM equations of a slightly curved pipe conveying fluid would be of the form

$$(M_p + M_f)\ddot{\underline{q}} + C_f \dot{\underline{q}} + (K_p + K_f)\underline{q} = \tilde{K}_f \underline{q}^{(0)} \tag{5.3}$$

where K_f and $\tilde{K}_f$ differ from each other by the axial preload effect if it is included. In this linear formulation, the pipe's undeformed curvature only affects the eigenvalues through the structural mass and stiffness matrices, M_p and K_p.

To validate this property, the normalized imaginary part of the first eigenvalue vs. normalized flow speed results presented in [15] were considered. They relate to a simply

supported curved pipe in the form of a half-sine wave of amplitude a_0 equal to 0, 1%, 2.5%, and 5% of the pipe length, see Fig. 34 Per the above discussion, the difference between the four curves should solely be the effects of the change in structural stiffness and mass resulting from the curvature. Thus, if a straight pipe ROM was calibrated to yield at zero flow the natural frequency of the curved pipe, a close agreement of the imaginary part of eigenvalue vs. flow speed should be obtained throughout. To check this possibility, the Young's modulus of the straight pipe was modified to yield the correct natural frequency in the no flow case. Then, its eigenvalues with flow were computed and also plotted in Fig. 34 As can be seen from this figure, the very close matching of the "fit" curves (i.e., the straight pipe predictions with modified Young's modulus) with the "data" ones (from [15]), demonstrates that the above property holds.

Thus, a small curvature of the pipe does not induce any significant change in the fluid forces except the presence of the term on the right-hand-side of Eq. (5.3). If the uncertainty on this term needs to be modeled, it is proposed here that the components of the vector $\underline{q}^{(0)}$ be taken as independent, zero mean Gaussian random variables.

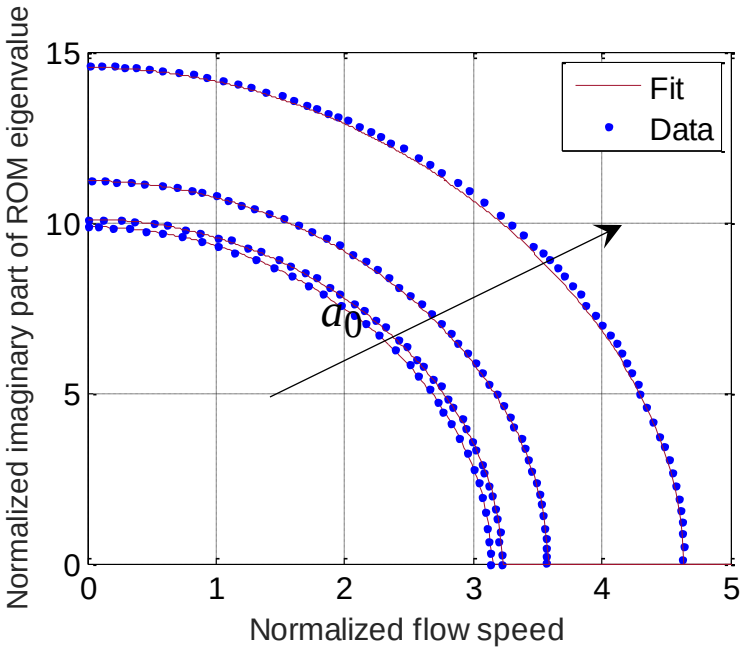

Figure 36. Normalized imaginary part of the first eigenvalue vs. normalized flow speed for curved pipes in the form of a half-sine wave of amplitude a_0 = 0, 1%, 2.5%, and 5% of the pipe length. Computations from [15] ("Data") and approximation based on calibrated straight pipe ("Fit")

REFERENCES

[1] Paidoussis, M.P. *Fluid-structure interactions slender structures and axial flow. Vol. 1*. Academic Press, Kidlington, Oxford, U.K., 2016.

[2] Ibrahim, R.A. "Overview of mechanics of pipes conveying fluids—Part I: Fundamental studies." *Journal of Pressure Vessel Technology*, Vol. 132, No. 3, 2010, 034001.

[3] Ibrahim, R. A. "Mechanics of pipes conveying fluids—Part II: Applications and fluidelastic problems." *Journal of Pressure Vessel Technology*, Vol. 133, No. 2, 2011, 024001.

[4] Hannoyer, M.J. *Instabilities of slender tapered tubular beams induced by internal and external axial flow*. PhD dissertation, McGill University, 1977.

[5] Hannoyer, M. J., and Paidoussis, M.P. "Dynamics of slender tapered beams with internal or external axial flow - Part 1: Theory." *Journal of Applied Mechanics*, Vol. 46, No. 1, 1979, pp. 45-51.

[6] Hannoyer, M. J., and Paidoussis, M.P. "Dynamics of slender tapered beams with internal or external axial flow - Part 2: Experiments." *Journal of Applied Mechanics*, Vol. 46, No. 1, 1979, pp. 52-57.

[7] Wang, L., Dai, H., and Ni, Q. "Mode exchange and unstable modes in the dynamics of conical pipes conveying fluid." *Journal of Vibration and Control*, Vol. 22, No. 4, 2016, pp. 1003-1009.

[8] Liu, Y., Zhang, Z., Li, B., and Gao, H. "Dynamic stiffness method for free vibration analysis of variable diameter pipe conveying fluid." *Journal of Vibroengineering*, Vol. 16, No. 2, 2014, pp. 832-845.

[9] Zhang, Z., Liu, Y., and Han, T. "Two parameters affecting the dynamics characteristics of a uniform-conical assembled pipe conveying fluid." *Journal of Vibration and Control*, Vol. 23, No. 3, 2017, pp. 361-372.

[10] Misra, A.K., Païdoussis, M.P., and Van, K.S. "On the dynamics of curved pipes transporting fluid. Part I: Inextensible theory." *Journal of Fluids and Structures*, Vol. 2, No. 3, 1988, pp. 221-244.

[11] Misra, A.K., Païdoussis, M.P., and Van, K.S. "On the dynamics of curved pipes transporting fluid. Part II: Extensible theory. " *Journal of Fluids and Structures*, Vol. 2, No. 3, 1988, pp. 245-261.

[12] Misra, A.K., Païdoussis, M.P., and Van, K.S. “Dynamics and stability of fluid conveying curved pipes.” *Proceedings of the International Symposium on Flow-Induced Vibration and Noise*, Chicago, IL, Vol. 4, 1988, pp. 1-24.

[13] Jung, D., and Chung, J. “A steady-state equilibrium configuration in the dynamic analysis of a curved pipe conveying fluid.” *Journal of Sound and Vibration*, Vol. 294, No. 1, 2006, pp. 410-417.

[14] Sinir, B.G. “Bifurcation and chaos of slightly curved pipes.” *Mathematical and Computational Applications*, Vol. 15, No. 3, 2010, pp. 490-502.

[15] Wang, L., Dai, H.L., and Qian, Q. “Dynamics of simply supported fluid-conveying pipes with geometric imperfections.” *Journal of Fluids and Structures*, Vol. 29, 2012, pp. 97-106.

[16] Ritto, T.G., Soize, C., Rochinha, F.A., and Sampaio, R. “Dynamic stability of a pipe conveying fluid with an uncertain computational model.” *Journal of Fluids and Structures*, Vol. 49, 2014, pp. 412-426.

[17] Soize, C. *Stochastic models of uncertainties in computational mechanics*. American Society of Civil Engineers, Reston, VA, 2012.

[18] Soize, C. “A nonparametric model of random uncertainties for reduced matrix models in structural dynamics.” *Probabilistic Engineering Mechanics*, Vol. 15, No. 3, 2000, pp. 277-294.

[19] Mignolet, M.P., Soize, C., and Avalos, J.. “Nonparametric stochastic modeling of structures with uncertain boundary conditions/coupling between substructures.” *AIAA Journal*, Vol. 51, No. 6, 2013, pp. 1296-1308.

[20] Durand, J.-F., Soize, C., and Gagliardini, L. “Structural-acoustic modeling of automotive vehicles in presence of uncertainties and experimental identification and validation.” *The Journal of the Acoustical Society of America*, Vol. 124, No. 3, 2008, pp. 1513-1525.

[21] Ohayon, R., and Soize, C. *Advanced computational vibroacoustics: reduced-order models and uncertainty quantification*. Cambridge University Press, Cambridge, U.K., 2014.

[22] Murthy, R., Mignolet, M.P., and El-Shafei, A. “Nonparametric stochastic modeling of uncertainty in rotordynamics - Part I: Formulation.” *Journal of Engineering for Gas Turbines and Power*, Vol. 132, No. 9, 2010, 092501.

[23] Murthy, R., Mignolet, M.P., and El-Shafei, A. “Nonparametric stochastic modeling of uncertainty in rotordynamics - Part II: Applications." ” *Journal of Engineering for Gas Turbines and Power*, Vol. 132, No. 9, 2010, 092502.

[24] Murthy, R., Tomei, J.C., Wang, X.Q., Mignolet, M.P., and El-Shafei, A.. “Nonparametric stochastic modeling of structural uncertainty in rotordynamics: unbalance and balancing aspects.” *Journal of Engineering for Gas Turbines and Power*, Vol. 136, No. 6, 2014, 062506.

[25] Mignolet, M.P., and Soize, C. “Stochastic reduced order models for uncertain geometrically nonlinear dynamical systems.” *Computer Methods in Applied Mechanics and Engineering*, Vol. 197, No. 45, 2008, pp. 3951-3963.

[26] Capiez-Lernout, E., Soize, C., and Mignolet, M.P.. “Post-buckling nonlinear static and dynamical analyses of uncertain cylindrical shells and experimental validation.” *Computer Methods in Applied Mechanics and Engineering*, Vol. 271, 2014, pp. 210-230.

[27] Song, P., Wang, X.Q., Matney, A., Murthy, R., and Mignolet, M.P.. "Nonlinear geometric thermoelastic response of structures with uncertain thermal and structural properties.” *Proceedings of the AIAA Science and Technology Forum and Exposition (SciTech 2017),* AIAA Paper 2017-0181.

[28] Soize, C., and Poloskov, I.E.. “Time-domain formulation in computational dynamics for linear viscoelastic media with model uncertainties and stochastic excitation.” *Computers & Mathematics with Applications*, Vol. 64, No. 11, 2012, pp. 3594-3612.

[29] Batou, A., and Soize, C.. “Rigid multibody system dynamics with uncertain rigid bodies.” *Multibody System Dynamics*, Vol. 27, No. 3, 2012, pp. 285-319.

[30] Richter, L.A., and Mignolet, M.P.. “Stochastic modeling of uncertain mass characteristics in rigid body dynamics.” *Mechanical Systems and Signal Processing*, Vol. 87, 2017, pp. 43-53.

[31] Soize, C. “Random matrix theory for modeling uncertainties in computational mechanics." *Computer Methods in Applied Mechanics and Engineering*, Vol. 194, No. 12, 2005, pp. 1333-1366.

[32] Fish, J., and Belytschko, T.. *A first course in finite elements*. 2007.

[33] Davis, P., and Rabinowitz, P.. “Abscissas and weights for Gaussian quadratures of high order.” *Journal of Research of the National Bureau of Standards*, Vol. 56, No. 1, 1956, pp. 35-37.

[34] Soize, C.. “Generalized probabilistic approach of uncertainties in computational dynamics using random matrices and polynomial chaos decompositions.” *International Journal for Numerical Methods in Engineering*, Vol. 81, No. 8, 2010, pp. 939-970.

[35] Avalos, J., Richter, L.A., Wang, X.Q., Murthy, R., and Mignolet, M.P.. “Stochastic modal models of slender uncertain curved beams preloaded through clamping.” *Journal of Sound and Vibration*, Vol. 334, 2015, pp. 363-376.

APPENDIX A

SUFFICIENT CONDITION FOR THE EIGENVALUES OF A DAMPED MULTI DEGREE OF FREEDOM TO BE PURELY IMAGINARY

Consider here the multi degree of freedom system satisfying the equations of motion

$$M\,\underline{\ddot{q}} + C\,\underline{\dot{q}} + K\,\underline{q} = \underline{0} \tag{A.1}$$

It is desired to prove that the corresponding free response is of the form

$$\underline{q} = \underline{\psi}\, e^{i\omega t} \tag{A.2}$$

with $\underline{\psi}$ independent of time and ω real if *M* and *K* are real symmetric, *M* is nonsingular, and *C* is real skew symmetric. To this end, introducing Eq. (A.2) into (A.1) leads to the quadratic eigenvalue problem

$$\left[-\omega^2 M + i\,\omega C + K\right]\underline{\psi} = \underline{0} \tag{A.3}$$

Next, let

$$\underline{\phi} = \begin{bmatrix} \underline{\psi} \\ \omega\,\underline{\psi} \end{bmatrix} \tag{A.4}$$

Then, Eq. (A.3) can be rewritten in the form

$$A\,\underline{\phi} = \omega B\,\underline{\phi} \tag{A.5}$$

where

$$A = \begin{bmatrix} K & 0 \\ 0 & M \end{bmatrix} \qquad \text{and} \qquad B = \begin{bmatrix} -i\,C & M \\ M & 0 \end{bmatrix} \tag{A.6}$$

Given their forms, it is readily seen that both *A* and *B* are Hermitian, i.e., $A^H = A$ and $B^H = B$, with ^{H} denoting the combined operation of complex conjugation and matrix transposition, when *M* and *K* are real symmetric and *C* is real skew symmetric. Then, pre-multiplying Eq. (A.5) by $\underline{\phi}^H$ it is seen that

$$\omega = \frac{\underline{\phi}^H A \underline{\phi}}{\underline{\phi}^H B \underline{\phi}} \tag{A.7}$$

but both numerator and denominator of this expression are purely real since A and B are Hermitian. Thus, the frequency ω is real.